Journal of Biomedical Optics

BiomedicalOptics.SPIEDigitalLibrary.org

Automated detection of the choroid boundary within OCT image data using quadratic measure filters

Marcus Wagner
Patrick Scheibe
Mike Francke
Beatrice Zimmerling
Katharina Frey
Mandy Vogel
Stephan Luckhaus
Peter Wiedemann
Wieland Kiess
Franziska G. Rauscher

SPIE.

Marcus Wagner, Patrick Scheibe, Mike Francke, Beatrice Zimmerling, Katharina Frey, Mandy Vogel, Stephan Luckhaus, Peter Wiedemann, Wieland Kiess, Franziska G. Rauscher, "Automated detection of the choroid boundary within OCT image data using quadratic measure filters," *J. Biomed. Opt.* **22**(2), 025004 (2017), doi: 10.1117/1.JBO.22.2.025004.

Automated detection of the choroid boundary within OCT image data using quadratic measure filters

Marcus Wagner,[a] Patrick Scheibe,[b,*] Mike Francke,[b,c] Beatrice Zimmerling,[b,c] Katharina Frey,[d] Mandy Vogel,[e] Stephan Luckhaus,[a,f] Peter Wiedemann,[g] Wieland Kiess,[e,h,i] and Franziska G. Rauscher[g]
[a]Max Planck Institute for Mathematics in the Sciences, Leipzig, Germany
[b]Leipzig University, Saxonian Incubator for Clinical Translation, Leipzig, Germany
[c]Leipzig University, Paul-Flechsig-Institute of Brain Research, Leipzig, Germany
[d]Ernst-Abbe-Hochschule Jena—University of Applied Sciences, Department SciTec, Jena, Germany
[e]Leipzig University, LIFE Leipzig Research Center for Civilization Diseases, Leipzig, Germany
[f]Leipzig University, Institute of Mathematics, Leipzig, Germany
[g]Leipzig University Hospital, Department of Ophthalmology, Leipzig, Germany
[h]University Hospital for Children and Adolescents and Center for Pediatric Research, Department of Women and Child Health, Leipzig University, Leipzig, Germany
[i]Leipzig University, Integrated Research and Treatment Center Adiposity Diseases, Leipzig, Germany

Abstract. A novel method for the automated detection of the outer choroid boundary within spectral-domain optical coherence tomography image data, based on an image model within the space of functions of bounded variation and the application of quadratic measure filters, is presented. The same method is used for the segmentation of retinal layer boundaries and proves to be suitable even for data generated without special imaging modes and moderate line averaging. Based on the segmentations, an automated determination of the central fovea region and choroidal thickness measurements for this and two adjacent 1-mm regions are provided. The quality of the method is assessed by comparison with manual delineations performed by five trained graders. The study is based on data from 50 children of the ages 8 to 13 that were obtained in the framework of the LIFE Child study at Leipzig University. [DOI: 10.1117/1.JBO.22.2.025004]

Keywords: spectral-domain optical coherence tomography; outer choroid boundary; automated detection; choroidal thickness; functions of bounded variation; quadratic measure filter.

Paper 160609R received Sep. 1, 2016; accepted for publication Jan. 3, 2017; published online Feb. 11, 2017.

1 Introduction

The choroid, a vascular structure between the retina and sclera, is primarily responsible for oxygenation and metabolic activity of the retinal pigment epithelium layer (RPE) and the outer retina. Its main substructures are (i) the Bruch's membrane; (ii) the choriocapillaris, a capillary network adjacent to the Bruch's membrane; (iii) the choroidal stroma, layers with intermediate and large vessels that drain the choriocapillaris; (iv) the suprachoroid, a transitional zone between the choroid and sclera ($\sim$30 μm thick) composed of numerous compactly arranged lamellae of melanocytes, fibroblasts, collagen bundles, and nerve fibers (for more details, see Refs. 1–3). Long-term variations of choroidal thickness occur in the process of infantile ocular development and healthy aging of adults[4,5] as well as in connection with retinal diseases, which can affect the choroid.[6,7] In the literature, short-term (even diurnal) thickness variations have been reported as well, cf. Ref. 2, pp. 154 ff.; Ref. 8. Differences in choroidal thickness have also been observed in relation to different levels of myopia.[9] Consequently, there is a considerable interest in accurate measurements of choroidal thickness.

Historically, the standard procedure for choroid imaging was indocyanine green angiography, which allows for two-dimensional (2-D) imaging of the choroid pattern and detection of leakage and vessel wall abnormalities.[10] Although optical coherence tomography (OCT) has become a standard tool for noninvasive imaging of the retinal layers since its introduction in 1991, its application for the investigation of the choroid has largely been unsuccessful for more than a decade. In OCT images, the (visual as well as automated) identification of the highly reflective RPE/choroid boundary is easy, but the detection of the outer choroid boundary (OCB) is a much more challenging task for several reasons. First, the position of the choroid posterior to the highly scattering layers of the cellular/subcellular structures of the outer retina causes a relatively weak signal from the region as a whole. Second, the observed reflectivity jumps are weak and strongly affected by noise. Only recent advances in OCT imaging, namely real-time eye-tracking (allowing for averaging of large numbers of A-scans), enhanced depth imaging (EDI SD-OCT) (as introduced in Ref. 11), swept-source OCT (SS-OCT)[12] or additional use of polarization information[13] led to high-quality *in vivo* visualizations of the choroidal vasculature, providing reliable depth information for choroidal thickness measurements. A third, principal difficulty results from the heterogeneous structure of the suprachoroidal layer, which consists of tightly interlaced components of both low and high reflectivity (melanocytes resp. collagen bands and fibroblasts).[3] As a consequence, it may be questioned whether the border between the suprachoroid and the collagen bundles of the sclera, which is histologically well-defined, is

*Address all correspondence to: Patrick Scheibe, E-mail: pscheibe@sikt.uni-leipzig.de

always clearly resolved by OCT imaging. Instead, the positive contrast jump visible in the data, which seems to be related to regions with sufficiently high concentrations of melanocytes, is used for the operational definition of the OCB in the present study (as well as in the vast majority of the literature), thus providing a reliable inner approximation of the histological choroid/sclera border.

The built-in segmentation routines in OCT devices are not suitable for scientific measurements as they are designed mainly for diagnostical purposes and, in general, are poorly documented (if at all). For the automated segmentation of retinal layers in OCT images, in particular for the detection of the RPE/choroid boundary, a large variety of scientifically documented methods is available by now. These include denoising by diffusion and subsequent edge detection,[14] denoising and simultaneous edge detection by variational methods,[15] active contour methods,[16] graph-theoretical approaches,[17–20] and classification by support vector machines.[21] Furthermore, in Ref. 22, a statistical segmentation method that is essentially based on the application of a neural network was proposed. Note that in almost all aforementioned cases a preceding denoising step is included even when not explicitly mentioned.

In contrast to this situation, the majority of studies concerned with the determination of choroidal thickness rely on manual or semi-manual detection of the OCB.[4–7,9,12,23–35] Unfortunately, manual delineation procedures are quite time-consuming and show considerable intra- and interobserver variability even when based on EDI SD-OCT or SS-OCT data.[28,36,37] Therefore, an automated detection of the OCB is highly desirable but has been realized only in a small number of studies until now, applying successful approaches for retinal layer segmentation to OCB detection. The studies[36,38–42] pursue graph-theoretical approaches while[43] adapted their statistical segmentation technique from their previous work.[22]

In the present study, we establish a novel method for the automated detection of the OCB within SD-OCT image data. In difference to the studies mentioned above, our approach is based on an image model within the space of functions of bounded variation (BV) and combines the application of quadratic measure filters[44–49] with elementary feature recognition. To the best of the authors' knowledge, the method has not been used in the context of medical image processing as yet. It applies to the detection of retinal layer boundaries as well and is particularly suitable for OCT data generated without special imaging modes (as EDI or SS-OCT) and moderate line averaging. To demonstrate the capability of the new approach, only such data (acquired without EDI module, 10 times averaged) were used in the present study. Note that a considerable number of OCT studies employ solely this low-grade image quality (certainly, the method presented applies to data of higher quality just as well, as will be shown in a subsequent publication). Within the B-scans, three layer boundaries were automatically recognized: the inner limiting membrane (ILM) boundary, the RPE/choroid boundary and the OCB. Based on these segmentations, we provide an automated determination of the central fovea region.[50,51] Automated measurements of mean choroidal thickness are given for this and two adjacent 1 mm regions, as defined in more detail in Sec. 2.6. The quality of the automated procedures will be assessed by comparison with manual segmentations performed by five trained graders and subsequent thickness derivations. Moreover, we shortly discuss whether the obtained OCB segmentations correspond to the histological structure of the transitional zone between the choroid and sclera, cf. Ref. 2, p. 147; Ref. 3. Our study is based on data from 50 children aged 8 to 13 years, which have been collected in the framework of the LIFE Child study at the Leipzig University.

The outline of the paper is as follows. In Sec. 2, we describe material and methods, particularly providing a detailed description of the automated segmentation method. Section 3 is devoted to the presentation and discussion of the results, Sec. 4 presents our conclusions. For convenience of the reader, the mathematical background of the presented method is briefly summarized in the Appendix. Detailed information about the OCT data is contained in Table 1.

2 Material and Methods

2.1 *Selection of Probands within the Framework of the LIFE Child Study*

The LIFE Child study is a population-based longitudinal cohort study conducted in Leipzig, a city in central Germany with more than 500,000 inhabitants. With recruitment age ranging between the 24th week of gestation and 16 years of age and annual follow-ups, the study combines a cross-sectional and a longitudinal design. Participants stem from the city of Leipzig and its close proximity. Recruitment started in 2011 and is planned to continue until 2021. By the end of 2015, more than 3000 children have already participated. Study participants are recruited via advertisement at different institutions such as university hospitals, local clinics, public health centers, kindergartens, schools, and partner study centers. The study program covers the collection of biological samples, examination of body functions and assessment of skills, traits, and habits (for more details, see Ref. 52). For the present work, OCT data from 50 children (25 male, 25 female) aged 8 to 13 have been randomly selected. The use of data was approved by the institutional review board of the Leipzig Research Center for Civilization Diseases (LIFE).

The LIFE Child study follows the tenets of the Declaration of Helsinki. Its outline was approved by the Ethics Committee of the Leipzig University (Reg. No. 264-10-19042010). The study has been registered with the trial number NCT02550236. The parents of the participating children were informed about the study program, the long-term use of data, potential risks of participation and the right to withdraw from the study. Written informed consent is obtained from the parents of all individual participants included in the study.

2.2 *Acquisition of SD-OCT Image Data*

Chorio-retinal images were obtained with a commercially available spectral-domain (SD) OCT (Spectralis HRA + OCT, equipped with camera head with serial number 04514, software modules Heidelberg Eye Explorer 1.7.0.0, Aquisition Module 5.4.7.0 and Viewing Module 5.4.6.0; Heidelberg Engineering, Heidelberg, Germany). The device uses a super luminescent diode with a central wavelength of 870 nm and acquires 40,000 A-scans/s. The scan depth in tissue is 1.9 mm with 496 pixels per A-scan, resulting in a pixel depth of 3.87 μm while the axial optical resolution amounts to 7 μm, cf. Ref. 53, p. 273. For each child, volume scans of the macular area with a field size of 20 deg (temporal-nasal) $\times$ 20 deg (superior-inferior) were acquired. Each volume scan contains 97 equally spaced averaged B-scans consisting of

Table 1 OCT data. Right eye imaged; size of B-scans is 496×512 px; pixel depth is 3.87 μm.

Subject no.	Fov. center at B-scan (no.)	Fovea pos. (px)	Gender	Age (y)	Mean ax. length (mm)	Scan focus (dpt)	Mean corneal rad. (mm)	Pixel width (μm)
01	50	256	Male	12.8	24.33	0.0275	7.90	11.40
02	49	244	Male	12.4	23.60	0.5600	7.90	11.30
03	50	257	Male	13.1	23.46	0.2600	7.85	11.31
04	50	256	Male	13.1	21.86	0.3300	7.60	11.07
05	50	260	Male	13.3	22.54	−0.5100	7.64	11.26
06	45	256	Female	12.6	22.10	−0.3800	7.35	10.96
07	49	236	Female	13.8	21.76	−0.0500	7.15	10.70
08	49	244	Female	13.6	23.35	0.4875	7.87	11.29
09	50	245	Female	13.3	22.97	−1.4275	8.01	11.79
10	50	252	Female	13.7	22.98	0.3400	7.57	11.04
11	49	259	Male	11.2	23.41	0.7900	8.04	11.38
12	53	248	Male	11.1	23.16	0.8800	7.69	11.05
13	49	256	Male	12.6	23.86	−1.0400	7.84	11.55
14	50	256	Male	12.6	23.35	0.2075	7.79	11.27
15	49	252	Male	11.1	23.47	1.1775	7.79	11.09
16	51	260	Female	11.6	23.28	−0.2000	7.61	11.17
17	48	243	Female	10.9	23.52	1.4000	7.69	10.96
18	50	251	Female	12.1	23.10	−0.0500	7.80	11.32
19	53	252	Female	11.0	23.02	−0.0875	7.65	11.19
20	49	251	Female	12.3	22.14	−0.0275	7.86	11.38
21	48	260	Male	10.7	23.62	−0.1300	7.76	11.30
22	49	276	Male	10.1	23.60	0.8675	7.90	11.24
23	45	245	Male	11.0	22.84	2.9300	7.67	10.68
24	50	248	Male	10.1	23.04	0.2600	7.66	11.14
25	49	256	Male	10.2	23.51	0.7175	7.88	11.25
26	48	256	Female	10.1	21.45	1.6100	7.25	10.52
27	50	252	Female	10.8	22.64	1.5600	7.73	10.97
28	49	236	Female	10.6	22.87	−1.1200	7.73	11.46
29	50	284	Female	10.5	21.80	4.4575	7.98	10.68
30	49	252	Female	10.5	22.55	0.1000	7.78	11.28
31	51	245	Male	9.2	22.18	0.5600	7.67	11.09
32	49	236	Male	9.7	22.93	1.4775	8.10	11.31
33	47	252	Male	9.4	20.89	0.0275	7.21	10.75

Table 1 (*Continued*).

Subject no.	Fov. center at B-scan (no.)	Fovea pos. (px)	Gender	Age (y)	Mean ax. length (mm)	Scan focus (dpt)	Mean corneal rad. (mm)	Pixel width (μm)
34	47	260	Male	10.5	22.66	−1.3900	7.65	11.44
35	50	245	Male	10.2	20.96	6.1900	7.95	10.37
36	47	245	Female	9.6	22.51	−0.9675	7.62	11.33
37	49	252	Female	9.4	23.23	−2.0400	7.26	11.16
38	49	259	Female	10.1	22.65	−0.7375	7.59	11.25
39	49	252	Female	9.7	22.81	0.1000	7.82	11.31
40	48	252	Female	9.2	22.34	0.4100	7.53	10.99
41	51	236	Male	8.5	24.02	0.2500	8.41	11.81
42	50	244	Male	8.6	23.79	0.9400	8.18	11.48
43	50	256	Male	9.2	21.50	−0.5775	7.31	10.95
44	49	252	Male	8.2	22.55	0.7900	7.64	11.02
45	46	240	Male	8.4	23.66	−0.0575	8.23	11.72
46	49	236	Female	8.2	22.04	0.7900	7.58	10.97
47	50	244	Female	8.4	20.72	6.7575	7.79	10.17
48	51	255	Female	8.1	22.23	0.6500	7.68	11.08
49	48	260	Female	8.4	22.22	0.0275	7.58	11.10
50	52	244	Female	8.3	22.61	−0.4275	7.73	11.33

496×512 pixels. Additionally, the device utilizes a confocal scanning laser ophthalmoscope at a wavelength of 815 nm to capture an overview image of the retina. Herein points are mapped to track eye movements using the overview image as a reference. This built-in function for real-time eye-tracking was active in order to obtain an average of 10 B-scans per line. EDI module was not used for the current analysis. For all children, both eyes were measured but the subsequent analysis was carried out on right eye data only. Corneal radii were measured with the Lenstar instrument (LS900 Biometer, Haag-Streit, Wedel, Germany). The median of three to six corneal biometry measurements was used for calculating the mean anterior corneal radius (included in Table 1) by averaging the steep and flat anterior meridians. Axial length was obtained as the mean of three to six measurements per eye, performed by the above mentioned Lenstar instrument. Measurement precision for corneal radii and axial length is about 0.01 mm, cf. Ref. 54, p. 13.

For the purpose of segmentation, exclusively the raw OCT data were exported and used.[55] Additionally, for convenience, a horizontal strip of 16×512 pixels with zero values was joined with each original B-scan. Using the results of the ILM and RPE/choroid boundary detection, from every volume scan, a B-scan defining the foveal center has been singled out (see Sec. 2.5). These scans have been further used for choroidal thickness measurements (see Table 1). A typical B-scan (Table 1, line 45) is shown in Fig. 1(a).

2.3 *Description and Implementation of the Edge Detection Method*

Basic approach. In order to detect a layer boundary within the OCT data I, the following five steps were performed: (1) smoothing of I by calculation of $(I * \varphi_\varepsilon)$, (2) calculation of discretized edge detectors $d_{\varepsilon,k}(i,j)$, (3) evaluation of the edge detectors by columnwise local maxima search (testing of the alternative expressed in Eq. (34), see Appendix), (4) preliminary estimation of the layer position according to its definition, and (5) final designation of the position by calculation of barycenters and cubic spline interpolation. In the following, the different steps will be reported in full detail.

Step 1. Convolution. The convolution $(I * \varphi_\varepsilon)$ with the scaled Gauss kernel $\varphi_\varepsilon(s) = (4\pi\varepsilon^2)^{-1} \cdot \exp[-|s|^2/(4\varepsilon^2)]$ is calculated as the numerical solution of the heat equation on the domain $\mathrm{Q} \times [0, \varepsilon^2]$ with initial values I, cf. Ref. 57, p. 47, Theorem 1. Specifying $Q = [-1,1]^2$, the edge length of a pixel is $1/256 = 0.003906$. Note that, at the same time, φ_ε is the density of the 2-D normal distribution with mean value $\mathfrak{o}_2$ and standard deviation $\sigma = \sqrt{2}\varepsilon$. Consequently, the 3σ region of φ_{ε_r} coincides with the ball centered in the origin $\mathfrak{o}_2$ and radius $r/256$ for $\varepsilon_r = r/(256 \cdot \sqrt{18})$, where $r \in \mathbb{N}$.

Step 2. Discretized edge detectors. Assuming that $Q = [-1,1]^2$ is subdivided into pixels $Q_{i,j}$, $1 \leqslant i \leqslant 512$, $1 \leqslant j \leqslant 512$, the test functions $\psi_5(i,j)(s)$, $\psi_7(i,j)(s) : Q \to \mathbb{R}$ are specified through

$$\psi_5(i,j)(s) = \begin{cases} s_2 + 2/256 \,| & (j-1-256)/256 \leqslant s_1 \leqslant (j-256)/256,\ (256-i-2)/256 \leqslant s_2 \leqslant (256-i+0.5)/256; \\ 3/256 - s_2 \,| & (j-1-256)/256 \leqslant s_1 \leqslant (j-256)/256,\ (256-i+0.5)/256 \leqslant s_2 \leqslant (256-i+3)/256; \\ 0 \,| & \text{else}, 3 \leqslant i \leqslant 510, 1 \leqslant j \leqslant 512; \end{cases} \quad (1)$$

$$\psi_7(i,j)(s) = \begin{cases} s_2 + 3/256 \,| & (j-1-256)/256 \leqslant s_1 \leqslant (j-256)/256,\ (256-i-3)/256 \leqslant s_2 \leqslant (256-i+0.5)/256; \\ 4/256 - s_2 \,| & (j-1-256)/256 \leqslant s_1 \leqslant (j-256)/256,\ (256-i+0.5)/256 \leqslant s_2 \leqslant (256-i+4)/256; \\ 0 \,| & \text{else}, 4 \leqslant i \leqslant 509, 1 \leqslant j \leqslant 512 \end{cases} \quad (2)$$

$\psi_5(i,j)$ and $\psi_7(i,j)$ are supported on features $\Omega_5(i,j)$ and $\Omega_7(i,j)$ consisting of five or seven vertically adjacent pixels, respectively. Following the strategy described in Appendix A.3, six different edge detectors $d_{5,8}$, $d_{5,9}$, $d_{5,10}$, $d_{7,10}$, $d_{7,11}$, and $d_{7,12}$ ("quadratic measure filters") are defined as discretizations of the integrals

$$d_{k,r}(i,j) \approx \int_{\Omega_k(i,j)} \psi_k(i,j)(s) \cdot \varepsilon_r |\nabla(I * \varphi_{\varepsilon_r})(s)|^2 \mathrm{d}s, \quad (3)$$

with $k \in \{5,7\}$, $r \in \{8,9,10,11,12\}$, and $\varepsilon_r \in \{0.007366, 0.008286, 0.009207, 0.010128, 0.011049\}$.

Steps 3–5. Recognition of the ILM boundary. The vertical column of pixels (A-scan) at the position j is denoted by $A(j) = \bigcup_{1 \leqslant i \leqslant 512} Q_{i,j}$. For each of the three detectors $d_{5,r}$, within the sets $A(j) \cap \{s \in Q \,|\, \partial(I * \varphi_{\varepsilon_r})(s)/\partial s_2 \geqslant 0\}$, all local maxima are determined. Their positions are stored within sets $S^+_{5,r}$. Next, every marked pixel $Q_{i,j}$ within $S^+_{5,r}$ is replaced by the vertical three-pixel feature $Q_{i-1,j} \cup Q_{i,j} \cup Q_{i+1,j}$. Then the ILM boundary will be preliminary defined as the topmost adjacent feature within $S^+_{5,8} \cup S^+_{5,9} \cup S^+_{5,10}$ of sufficiently large size, marking a positive contrast jump. Denoting this feature by $F^+ \subset Q$, for the three edge detectors, the barycenters over $A(j) \cap F^+$ are calculated, and the mean of the three quantities is formed. The final position $\mathrm{ILM}_a(j)$ is obtained by cubic spline interpolation of the refined data.

Steps 3–5. Recognition of the RPE/choroid boundary. For each of the six detectors $d_{k,r}$, the local maxima over the sets $A(j) \cap \{s \in Q \,|\, \partial(I * \varphi_{\varepsilon_r})(s)/\partial s_2 < 0\}$ are determined. Their positions are stored within sets $S^-_{k,r}$. Every marked pixel $Q_{i,j}$ within $S^-_{k,r}$ is replaced by a cross-shaped feature $Q_{i-1,j} \cup Q_{i,j-1} \cup Q_{i,j} \cup Q_{i,j+1} \cup Q_{i+1,j}$. Then the RPE/choroid boundary will be preliminary defined as the lowermost adjacent feature within $S^-_{7,12} \cup S^-_{7,11} \cup S^-_{7,10} \cup S^-_{5,10} \cup S^-_{5,9} \cup S^-_{5,8}$ of sufficiently large size, marking a negative contrast jump at the same time. Denoting this feature by $F^- \subset Q$, for every edge detector, the barycenters over $A(j) \cap F^-$ are calculated. Forming the mean of the six quantities, a refined boundary position is obtained. Again, the final position $\mathrm{RPE}_a(j)$ is found by cubic spline interpolation of these data.

Steps 3–5. Detection of the OCB. Within the usual visualization of the B-scans, this boundary can be visually recognized as a fairly weak positive contrast jump below the RPE/choroid boundary [see Fig. 1(a)]. One may observe that this jump corresponds to a (possibly not connected) feature within the normalized gradient field of $(I * \varphi_\varepsilon)$ where the second component of the gradient vector is nonnegative [see Figs. 1(c) and 1(d)]. Consequently, the maximization of the edge detector will be restricted to a set Q^c, which is defined as the union of topmost connected features below the RPE/choroid boundary with

$$\frac{\partial}{\partial s_2}(I * \varphi_{\varepsilon_r})(s) \cdot |\nabla(I * \varphi_{\varepsilon_r})(s)|^{-1} \geqslant -\eta, \quad (4)$$

where $r = 10$ and $\eta = -1/10$. For the detector $d_{5,10}$, the local maxima over the sets $A(j) \cap Q^c$ are determined (these are situated below the RPE/choroid boundary by definition), and their positions are stored within a set $S^c_{5,10}$. Again, every marked pixel $Q_{i,j}$ within $S^c_{5,10}$ is replaced by a vertical three-pixel feature $Q_{i-1,j} \cup Q_{i,j} \cup Q_{i+1,j}$. Subsequently, all adjacent features smaller than 16 px are removed from $S^c_{5,10}$. Thus, a possibly unconnected feature F^c, which represents the coarse position of the lower choroid boundary, is obtained [see Fig. 2(a)]. This position is refined in two steps: after calculating the barycenters of $d_{5,10}$ over $A(j) \cap F^c$, the final position $\mathrm{OCB}_a(j)$ is obtained again by cubic spline interpolation.

Remarks about the implementation. The complete edge detection procedure was implemented as a series of MATLAB® tools. It was performed with MATLAB® 8.4.0.150421 (R2014b) and required the Image Processing and Signal Processing toolboxes, as documented in Refs. 58–60. For the numerical solution of the heat equation, after the introduction of a spatial mesh whose nodes are the centers of the pixels $Q_{i,j}$, the ADI method proposed by Peaceman/Rachford was employed, cf. Ref. 61, p. 412 f. Note that the missing smoothness of the initial values I does not influence the calculations. For the calculation of $d_{k,r}$ and feature recognition, the `imfilter` and `bwlabel` procedures were used while the maxima search was realized with the aid of the `findpeaks` procedure. The typical CPU time for the segmentation of a single B-scan amounts to 7.5 s (steps 2 to 5). No particular attempts for tuning have been made.

2.4 *Validation of the Computer-Generated Results*

The accuracy of the automated detection of the boundary layer positions has been validated by comparison with manual segmentation. To this end, within each of the 50 B-scans from Table 1, the ILM boundary, the RPE/choroid boundary, and the OCB were manually delineated by five trained graders (Anna Xenia Bestehorn, Mike Francke, Anja Schirmer, Sophia Scheibe and Beatrice Zimmerling) independently from each other, employing the usual visualization $\sqrt[4]{I}$ of the OCT data I, cf. Ref. 55, p. 11. The graders were allowed to enhance the contrast within the images if necessary. The manually obtained boundary positions will be denoted by $\mathrm{ILM}_1(j), \ldots, \mathrm{ILM}_5(j)$, $\mathrm{RPE}_1(j), \ldots, \mathrm{RPE}_5(j)$, and $\mathrm{OCB}_1(j), \ldots, \mathrm{OCB}_5(j)$, respectively. In Sec. 3.1, the comparison between manually and automatically obtained data is described in detail.

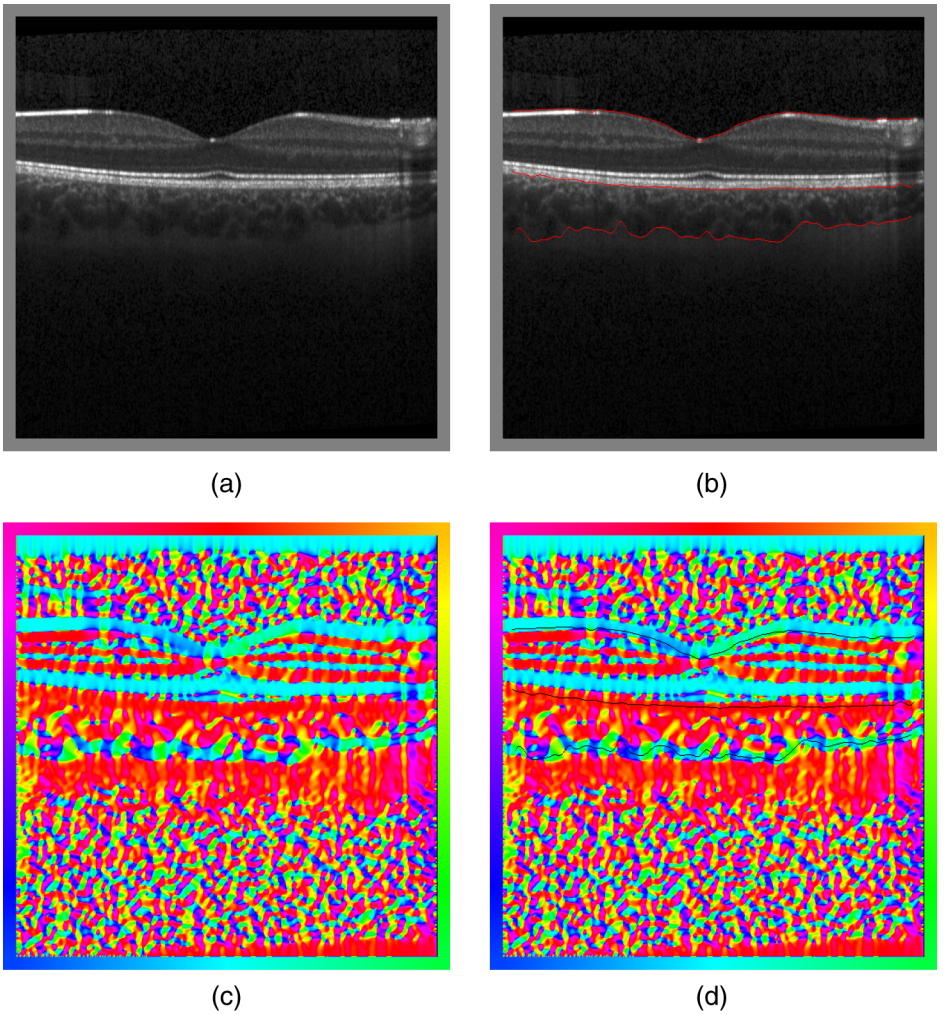

Fig. 1 Typical example of automated layer detection. (a) Original SD-OCT data (see Table 1, subject No. 45, B-scan No. 46 with foveal center) visualized as $\sqrt[4]{I}$. (b) Automatically detected ILM, RPE, and outer choroid boundaries superimposed to the B-scan as red curves. (c) Normalized gradient field of $(I * \varphi_{\varepsilon_{10}})$ visualized as colorful orientation plot, cf. Ref. 56, p. 1197. The gradient direction is coded by the color of a pixel; the correspondence between color and orientation can be read from the colored border as a legend. (d) Boundaries from (b) superimposed to the orientation plot (c) as black curves.

2.5 *Definition of the Foveal Region within the B-Scans*

Within each volume, the segmentation procedure was applied to the B-scans # 42 ... # 57. Subsequently, from each volume the minimal distance $\mathrm{ILM}_a(j) - \mathrm{RPE}_a(j)$ of the ILM and RPE/choroid boundaries, compared over the A-scans with numbers $200 \leqslant j \leqslant 312$, was extracted together with its position, thus defining the foveal center. The respective scan was singled out for further analysis (see Table 1).

In order to define within each of these scans the central fovea region, we rely on a fovea model introduced in Ref. 50. Following the procedure described there, a model function $\mathcal{M}(r)$ for the fovea shape was generated from the automatically extracted ILM and RPE boundary data and the position of the foveal center. The extent of the fovea bowl left and right from the center is given by two radii r_{left} and r_{right} that can be determined from the model $\mathcal{M}(r)$ (see Fig. 3). As pointed out in Ref. 51, p. 5, instead of using of the highest point of the foveal rim for this purpose, it is more advantageous to solve the equation

$$r_{\mathrm{left}} \cdot \mathcal{M}(r_{\mathrm{left}}) - \int_0^{r_{\mathrm{left}}} \mathcal{M}(r)\mathrm{d}r = p \cdot \mathcal{A}_{\mathrm{bowl,left}}, \tag{5}$$

with a percentage of $p = 0.95$ where the (one-sided) foveal bowl area

$$\mathcal{A}_{\mathrm{bowl,left}} = \int_0^{r_{\mathrm{rim,left}}} \mathcal{M}(r)\mathrm{d}r, \tag{6}$$

is calculated by integrating the model function until the highest point $r_{\mathrm{rim,left}}$ of the left foveal rim. Equation (5) was solved by bisection. Analogously, r_{right} has been found. The radii r_{left} and r_{right}, which have been derived from the automatically generated boundary positions ILM_a and RPE_a, were used throughout the whole following analysis.

Three choroid measurement regions were defined: (1) the central foveal zone, which is the region between r_{left} and r_{right}, (2) the 1-mm region left of the central foveal zone (corresponding to temporal retina for the right eyes examined), and (3) the 1-mm region right of the foveal zone (referring to the

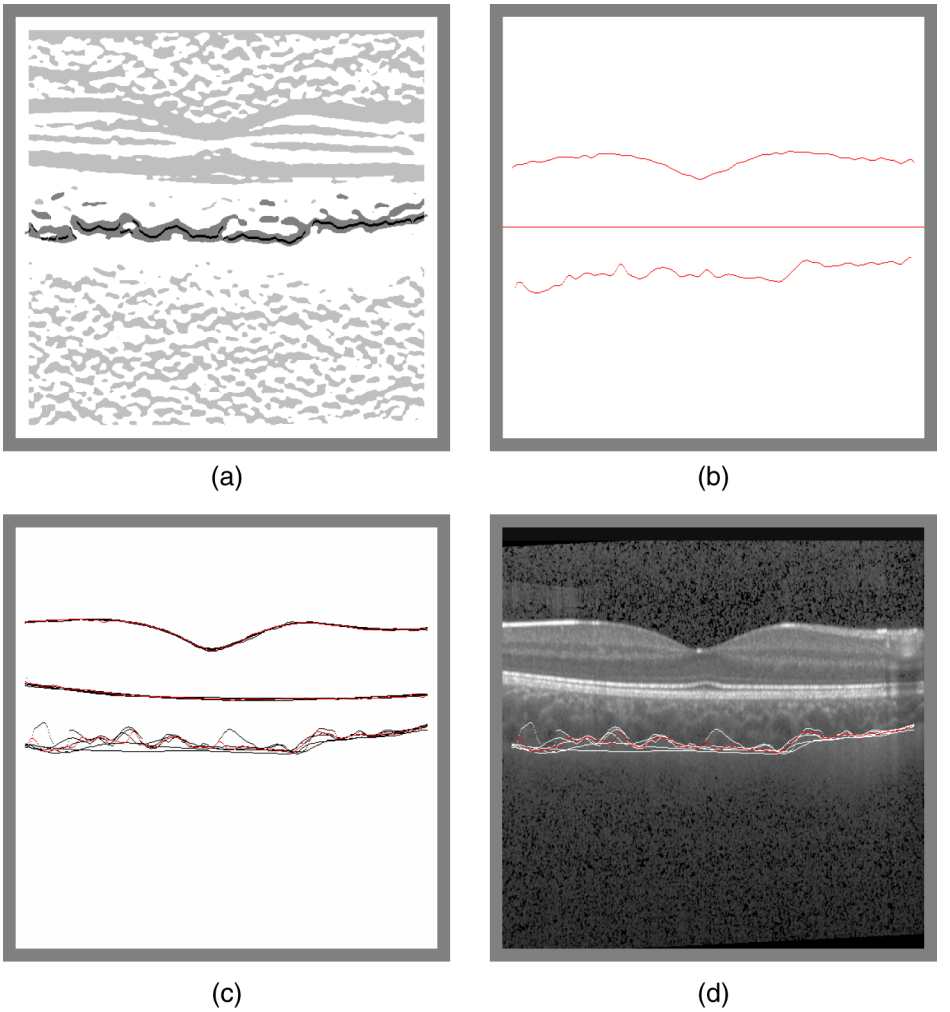

Fig. 2 Typical example of automated layer detection, continued. (a) Three steps of OCB detection visualized. The pixels satisfying inequality (4) are shown in light gray, the subset Q^c of topmost connected features below the RPE/choroid boundary is shown in dark gray, and the preliminary position F^c of the OCB is shown in black. (b) Plot of the relative positions of ILM and OCB with respect to the straightened RPE boundary line; results of automated detection. (c) Superposition of the five manual segmentations (black) and automated segmentation (red) of ILM, RPE, and OCB boundaries. (d) Superimposition of the original SD-OCT data, the five manual segmentations (white) and the automated segmentation (red) of the OCB. Same data as in Fig. 1(a) but differently visualized as $\sqrt[8]{I}$, thus revealing a significant level of speckle noise within the data.

nasal retina). As discussed in Ref. 51 in detail, one may observe a strong variability of foveal geometry between individuals, requiring the determination of a measurement region of variable width [thus the use of the standard 1 mm circle, which has been introduced in the context of fundus photography and is widely used in retinal thickness measurements (see Ref. 62, Chapter 18; Ref. 63), would be completely inappropriate]. Outside of the foveal rim, the individual shape variation is far less prominent, allowing for the definition of measurement regions of fixed dimensions. In order to obtain the magnification factor q that is directly used to calculate the pixel width in mm, we employed the formula published in Ref. 64, p. 649,

$$q = 17.455 \cdot [300.3(r_{\text{corn}})^{-1} + 21.76 + f_{\text{scan}}]^{-1}, \tag{7}$$

instead of the built-in but undocumented routine of the OCT device. Within Eq. (7), r_{corn} denotes the mean corneal radius in mm and f_{scan} the scan focus in dpt.

2.6 *Definition and Measurement of Choroidal Thickness*

The (pointwise) choroidal thickness is understood as the vertical distance from the hyperreflective line of the RPE/Bruch's membrane boundary to the positive contrast jump below this curve, which operationally defines the OCB as mentioned above. Within the three foveal regions defined in Sec. 2.5, the mean choroidal thicknesses are defined as

$$\text{CHL}_a = 1\ \text{mm}^{-1} \int_{(r_{\text{left}} - 1\ \text{mm})}^{r_{\text{left}}} |\text{RPE}_a(s_1) - \text{OCB}_a(s_1)| \text{d}s_1 \tag{8}$$

(left 1-mm region),

$$\text{CHC}_a = (r_{\text{right}} - r_{\text{left}})^{-1} \int_{r_{\text{left}}}^{r_{\text{right}}} |\text{RPE}_a(s_1) - \text{OCB}_a(s_1)| \text{d}s_1 \tag{9}$$

(central region) and

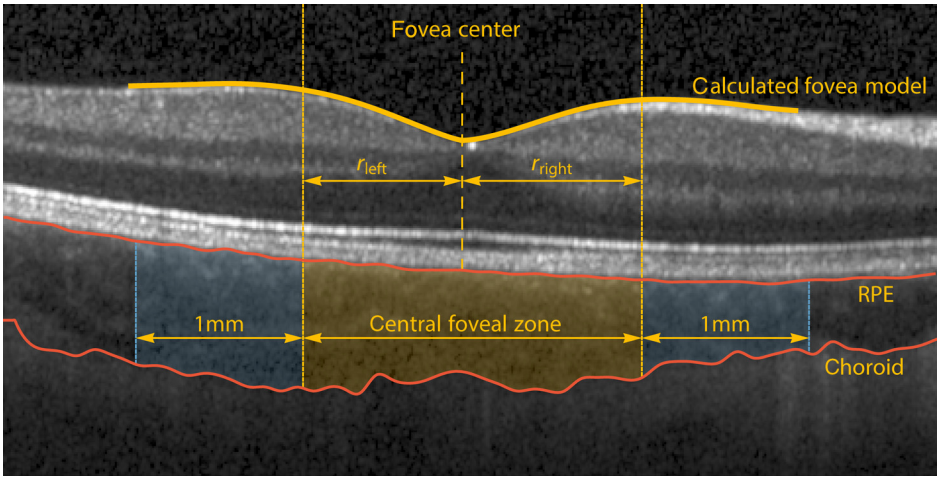

Fig. 3 Choroid thickness quantification procedure. Inscribed RPE and OCB layers were automatically extracted. ILM layer replaced by foveal model $\mathscr{M}(r)$ left and right from the fovea center, which has been computed as in 50. Based on the fovea model, left and right bowl radii were calculated as described in the text. The region between the radii defines an individual central foveal zone for each subject. Additionally, two outer 1-mm regions were defined, thus obtaining three zones where the mean choroidal thickness was assessed.

$$\mathrm{CHR}_a = 1\ \mathrm{mm}^{-1} \int_{r_{\mathrm{right}}}^{(r_{\mathrm{right}}+1\ \mathrm{mm})} |\mathrm{RPE}_a(s_1) - \mathrm{OCB}_a(s_1)|\mathrm{d}s_1, \tag{10}$$

(right 1-mm region). Numerical values for the above integrals were obtained by interpolating the data smoothly and applying a numerical integration procedure.

2.7 *Histological Examination of the Transitional Zone between Choroid and Sclera*

After enucleation, human donor eyes were fixed in 4% paraformaldehyde phosphate-buffered solution (PBS) for more than 24 h. Choroidal and scleral tissues were stored in PBS and prepared for light microscopy. Layers of choroidal stroma (Sattler's and Haller's layer) were partly removed to get a plane view onto the inner surface of the outer choroid. Plane view and cross-sectional images were obtained using a digital reflected-light microscope (VHX-600, Keyence Deutschland GmbH, Neu-Isenburg, Germany). Use of human tissue was approved by the Ethics Committee of the Leipzig University.

3 Results and Discussion

3.1 *Results of the Automated ILM, RPE, and OCB Boundary Detection*

In Table 2, we display the results of automated ILM and RPE detection. For every B-scan examined, the pointwise mean and the pointwise standard deviation of the five manual delineations is calculated as $\mathrm{ILM}_m(j) = \sum_{k=1}^{5} \mathrm{ILM}_k(j)/5$, $\mathrm{RPE}_m(j) = \sum_{k=1}^{5} \mathrm{RPE}_k(j)/5$, $\mathrm{ILM}_\sigma(j) = \sqrt{\sum_{k=1}^{5} \mathrm{ILM}_k(j)^2/5 - \mathrm{ILM}_m(j)^2}$, and $\mathrm{RPE}_\sigma(j) = \sqrt{\sum_{k=1}^{5} \mathrm{RPE}_k(j)^2/5 - \mathrm{RPE}_m(j)^2}$, respectively. With the aid of these quantities, for every B-scan, the averaged standard deviations

$$\overline{\mathrm{ILM}}_\sigma = \sum_{j=17}^{496} \mathrm{ILM}_\sigma(j)/480 \tag{11}$$

and

$$\overline{\mathrm{RPE}}_\sigma = \sum_{j=17}^{496} \mathrm{RPE}_\sigma(j)/480 \tag{12}$$

of the five manual delineations are defined (columns 1 and 4). They will be compared with the mean absolute errors

$$\overline{\mathrm{ILM}}\text{-}|\Delta|_a^m = \sum_{j=17}^{496} |\mathrm{ILM}_m(j) - \mathrm{ILM}_a(j)|/480 \tag{13}$$

and

$$\overline{\mathrm{RPE}}\text{-}|\Delta|_a^m = \sum_{j=17}^{496} |\mathrm{RPE}_m(j) - \mathrm{RPE}_a(j)|/480 \tag{14}$$

(columns 2 and 5) as well as with the mean errors

$$\overline{\mathrm{ILM}}\text{-}\Delta_a^m = \sum_{j=17}^{496} [\mathrm{ILM}_m(j) - \mathrm{ILM}_a(j)]/480 \tag{15}$$

and

$$\overline{\mathrm{RPE}}\text{-}\Delta_a^m = \sum_{j=17}^{496} [\mathrm{RPE}_m(j) - \mathrm{RPE}_a(j)]/480 \tag{16}$$

(columns 3 and 6), thus examining within the OCT data in all cases the A-scans with numbers $17 \leqslant j \leqslant 496$.

The results for the OCB are presented in Table 3. Again, for every B-scan examined, the pointwise mean and the pointwise standard deviation of the five manual delineations is calculated as $\mathrm{OCB}_m(j) = \sum_{k=1}^{5} \mathrm{OCB}_k(j)/5$ and $\mathrm{OCB}_\sigma(j) = \sqrt{\sum_{k=1}^{5} \mathrm{OCB}_k(j)^2/5 - \mathrm{OCB}_m(j)^2}$. Then for every B-scan the averaged standard deviation

Table 2 Results of automated ILM and RPE detection. Entries defined in Eqs. (11)–(16).

No.	$\overline{\text{ILM}}_\sigma$ (μm)	$\overline{\text{ILM}}$-$\lvert\Delta\rvert_a^m$ (μm)	$\overline{\text{ILM}}$-Δ_a^m (μm)	$\overline{\text{RPE}}_\sigma$ (μm)	$\overline{\text{RPE}}$-$\lvert\Delta\rvert_a^m$ (μm)	$\overline{\text{RPE}}$-Δ_a^m (μm)
01	2.54	2.76	+0.17	2.04	8.02	−6.55
02	3.86	2.93	+0.76	2.91	4.64	−2.13
03	3.37	3.56	+0.66	2.44	6.03	−5.56
04	3.47	3.71	+0.38	3.22	3.84	+2.58
05	2.81	3.43	−0.15	2.53	1.94	−0.01
06	2.66	3.40	+1.10	2.75	8.94	−8.88
07	2.60	2.86	−0.62	2.94	7.48	−6.83
08	3.02	3.05	+0.28	2.52	3.78	−0.93
09	2.51	3.31	+0.59	3.33	15.86	−15.61
10	2.94	2.21	−0.81	3.73	6.53	−6.18
11	2.90	3.64	−0.63	3.54	16.92	−16.69
12	2.67	3.02	+1.60	3.24	4.25	+4.16
13	3.97	2.91	−0.85	2.74	4.31	−3.50
14	2.82	3.29	+1.78	3.03	2.80	−1.49
15	3.17	3.66	+0.59	2.97	14.36	−14.17
16	3.35	3.51	+1.15	2.80	5.03	+4.98
17	3.30	3.37	−0.34	2.88	6.58	−5.74
18	3.25	4.37	+1.41	3.12	14.96	−14.96
19	2.89	3.96	+0.05	2.75	2.74	−2.10
20	2.84	3.45	−0.93	3.77	11.43	−10.69
21	3.53	3.13	−0.96	3.48	10.11	−9.74
22	2.94	2.43	+0.10	2.93	7.55	−7.20
23	3.19	3.34	+1.44	4.70	6.74	+6.74
24	2.76	3.19	−1.07	4.35	7.14	−6.90
25	3.06	2.53	+0.45	3.15	9.06	−9.00
26	2.64	3.50	−1.99	2.80	8.60	−7.52
27	2.79	3.16	−0.81	3.33	9.92	−4.22
28	2.89	3.52	+0.60	2.84	5.92	−3.18
29	2.37	2.30	−0.51	3.83	6.02	−4.66
30	2.76	3.66	−0.83	3.94	4.07	−2.39
31	2.57	2.17	−0.50	8.84	2.08	+1.52
32	2.46	4.07	+0.17	2.44	14.53	−13.83
33	2.82	3.98	−3.44	3.24	9.99	−7.75
34	3.14	3.09	+0.80	2.97	5.30	+5.30
35	2.66	2.55	+1.17	2.90	3.43	+3.37
36	2.50	3.40	−1.46	3.53	11.02	−11.02
37	3.02	2.98	−0.47	4.16	4.52	+4.27
38	2.85	3.41	−0.26	2.44	5.44	+5.43
39	2.90	3.21	−0.40	3.63	5.12	−3.48
40	3.51	3.54	−0.65	3.11	5.03	−3.07
41	2.48	3.40	+0.52	2.57	7.59	−7.29
42	2.39	3.52	+0.65	2.87	5.10	+4.91
43	2.94	3.85	−1.36	3.11	9.51	−9.50
44	2.62	3.25	−1.10	3.33	9.30	−8.19
45	2.55	2.86	+0.38	3.17	3.16	−0.65
46	2.50	2.76	−1.64	3.13	6.97	−6.93
47	2.96	2.83	+0.28	3.31	6.62	−4.40
48	3.08	2.87	+0.00	2.56	4.22	+0.70
49	2.53	3.69	+0.26	3.67	6.68	−6.54
50	2.98	3.16	+0.26	2.62	7.08	−6.87

$$\overline{\text{OCB}}_\sigma = \sum_{j=17}^{496} \text{OCB}_\sigma(j)/480, \tag{17}$$

of the five manual segmentations is defined (column 1), which is compared with the mean absolute error

$$\overline{\text{OCB}}\text{-}\lvert\Delta\rvert_a^m = \sum_{j=17}^{496} \lvert\text{OCB}_m(j) - \text{OCB}_a(j)\rvert/480, \tag{18}$$

and the absolute error

$$\overline{\text{OCB}}\text{-}\Delta_a^m = \sum_{j=17}^{496} [\text{OCB}_m(j) - \text{OCB}_a(j)]/480 \tag{19}$$

(columns 2 and 3). The percentage of the A-scans with numbers $17 \leqslant j \leqslant 496$ satisfying the inclusion $\text{Min}_{1\leqslant k\leqslant 5}\text{OCB}_k(j) \leqslant \text{OCB}_a(j) \leqslant \text{Max}_{1\leqslant k\leqslant 5}\text{OCB}_k(j)$ is given in column 4. Further, in columns 5 to 9, the mean absolute errors

$$\overline{\text{OCB}}\text{-}\lvert\Delta\rvert_a^k = \sum_{j=17}^{496} \lvert\text{OCB}_k(j) - \text{OCB}_a(j)\rvert/480, \quad 1 \leqslant k \leqslant 5, \tag{20}$$

for each single manual delineation are tabulated.

Table 3 Results of automated OCB detection. Entries defined in Eqs. (17)–(20).

No.	$\overline{\mathrm{OCB}}_{\sigma}$ (μm)	$\overline{\mathrm{OCB}}$-$\lvert\Delta\rvert_a^m$ (μm)	$\overline{\mathrm{OCB}}$-Δ_a^m (μm)	Perc. (%)	$\overline{\mathrm{OCB}}$-$\lvert\Delta\rvert_a^1$ (μm)	$\overline{\mathrm{OCB}}$-$\lvert\Delta\rvert_a^2$ (μm)	$\overline{\mathrm{OCB}}$-$\lvert\Delta\rvert_a^3$ (μm)	$\overline{\mathrm{OCB}}$-$\lvert\Delta\rvert_a^4$ (μm)	$\overline{\mathrm{OCB}}$-$\lvert\Delta\rvert_a^5$
01	19.43	10.76	+1.21	92.3	31.81	15.61	16.16	16.61	15.36
02	17.44	9.12	−6.73	93.1	22.59	23.44	10.48	13.81	16.12
03	35.45	25.63	−2.14	83.3	30.87	44.96	39.58	27.62	36.15
04	9.91	8.13	−4.85	78.8	9.86	12.40	8.21	11.29	15.04
05	30.53	26.40	−20.73	69.0	36.51	61.28	18.56	21.88	38.42
06	101.18	55.13	+51.06	95.6	170.24	50.42	175.39	27.34	28.09
07	99.08	32.02	−29.49	97.7	136.55	137.04	21.39	35.55	109.16
08	49.70	30.76	+4.80	81.0	69.27	24.60	27.87	64.05	17.82
09	81.60	59.64	−2.24	90.6	86.79	75.27	119.77	67.78	68.17
10	70.87	35.62	+7.56	91.9	93.41	64.22	70.19	82.46	37.35
11	42.05	51.68	−43.99	65.4	56.67	86.06	46.08	36.40	88.95
12	22.80	21.11	−17.80	76.0	23.85	37.45	19.84	20.12	42.11
13	28.21	31.34	−29.13	77.3	30.66	58.02	38.87	17.78	44.04
14	73.83	106.27	+37.12	64.6	191.94	81.92	174.63	64.16	106.02
15	25.66	12.24	−4.58	87.3	14.86	50.46	12.02	10.35	21.31
16	14.29	15.78	−5.71	75.6	21.20	27.67	18.06	17.22	18.06
17	16.71	14.40	−5.44	77.1	13.14	24.57	18.74	21.17	17.43
18	82.84	45.20	−29.51	87.7	53.88	106.18	111.28	93.03	96.76
19	56.80	52.08	−28.39	74.4	71.72	119.93	45.15	56.20	56.35
20	95.49	70.67	+4.41	90.6	152.10	120.56	189.80	58.19	55.21
21	79.38	52.35	−14.18	87.5	133.93	103.62	44.13	87.55	47.37
22	31.81	16.83	+10.16	95.6	23.31	16.78	63.91	13.88	14.28
23	33.50	41.80	−27.08	89.8	66.43	52.98	36.37	51.13	63.31
24	45.34	17.62	+9.50	97.7	88.34	30.84	21.80	18.25	24.74
25	47.91	31.74	−6.98	96.7	110.18	54.89	32.15	34.16	33.78
26	49.06	56.27	+33.63	65.2	100.53	46.25	65.99	70.20	45.40
27	9.74	4.71	−1.58	96.9	9.88	10.95	8.00	11.66	8.72
28	14.14	15.34	−11.61	70.0	14.36	30.78	11.32	16.40	22.61
29	53.46	24.30	+11.82	80.8	110.75	35.28	27.63	22.90	21.53
30	18.13	11.73	−2.30	76.9	15.41	26.29	12.89	22.32	8.75
31	36.09	145.45	−141.29	67.9	137.38	183.52	138.50	127.66	173.61
32	32.94	34.73	−25.91	75.0	34.89	63.72	38.29	27.72	55.38
33	20.38	12.19	+2.69	91.5	26.86	22.71	14.20	18.10	18.04
34	16.74	13.62	−13.27	81.7	8.84	40.19	11.77	10.92	18.98

Table 3 (*Continued*).

No.	$\overline{\text{OCB}}_\sigma$ (μm)	$\overline{\text{OCB}}$-$\lvert\Delta\rvert_a^m$ (μm)	$\overline{\text{OCB}}$-Δ_a^m (μm)	Perc. (%)	$\overline{\text{OCB}}$-$\lvert\Delta\rvert_a^1$ (μm)	$\overline{\text{OCB}}$-$\lvert\Delta\rvert_a^2$ (μm)	$\overline{\text{OCB}}$-$\lvert\Delta\rvert_a^3$ (μm)	$\overline{\text{OCB}}$-$\lvert\Delta\rvert_a^4$ (μm)	$\overline{\text{OCB}}$-$\lvert\Delta\rvert_a^5$
35	101.07	34.70	+19.21	86.7	149.78	54.40	124.42	48.62	96.06
36	69.38	50.03	+26.85	82.5	90.92	102.55	64.84	52.92	53.91
37	61.32	57.99	−32.76	87.7	57.72	97.09	63.39	75.64	65.95
38	70.89	58.78	+10.89	87.1	157.27	76.16	83.02	55.42	49.53
39	56.17	27.65	+9.62	96.5	93.70	64.94	28.25	32.69	35.13
40	30.96	49.43	+8.05	68.0	43.16	50.22	76.39	40.63	63.05
41	23.62	24.80	−20.31	95.0	34.32	55.11	24.94	27.06	30.80
42	16.62	10.02	+5.06	92.3	18.17	16.64	14.64	18.74	19.25
43	44.48	24.04	+19.12	87.9	56.44	59.86	58.31	22.29	29.16
44	58.58	45.86	−27.30	77.1	30.02	120.18	44.32	31.46	82.59
45	18.41	10.02	−4.34	93.8	15.83	18.71	10.88	14.98	25.58
46	29.15	24.99	+20.21	81.7	33.18	19.46	33.74	46.38	29.90
47	52.34	63.48	−61.68	77.9	20.88	83.21	35.46	114.77	99.50
48	25.39	16.42	+6.75	85.6	30.85	17.31	20.52	28.69	29.98
49	9.21	6.78	−5.56	78.3	8.40	13.36	5.34	7.93	16.72
50	53.44	90.34	−56.10	64.8	86.74	112.44	97.11	95.02	103.12

3.2 *Results of the Automated Choroidal Thickness Measurements*

In Table 4, the choroidal thickness measurements for the central foveal region are presented. For comparison, we determined for every B-scan from the five manual delineations RPE_k and OCB_k the thicknesses

$$\text{CHC}_k = (r_{\text{right}} - r_{\text{left}})^{-1} \int_{r_{\text{left}}}^{r_{\text{right}}} |\text{RPE}_k(s_1) - \text{OCB}_k(s_1)| \text{d}s_1, \quad 1 \leqslant k \leqslant 5, \tag{21}$$

using the radii r_{left} and r_{right} obtained from the automated segmentations and the same procedures as mentioned in Sec. 2.5. For every B-scan, the five values CHC_k obtained from the manual delineations are tabulated in columns 1 to 5. Columns 6 and 7 contain the mean

$$\text{CHC}_m = \sum_{k=1}^{5} \text{CHC}_k / 5, \tag{22}$$

and the standard deviation

$$\text{CHC}_\sigma = \sqrt{\sum_{k=1}^{5} \text{CHC}_k^2 / 5 - \text{CHC}_m^2} \tag{23}$$

of the five values before. The result CHC_a of the automated measurement and the error

$$\text{CHC-}\Delta_a^m = \text{CHC}_m - \text{CHC}_a \tag{24}$$

are given in columns 8 and 9. Table 5 contains the choroidal thickness measurements for the left and right 1-mm regions. Analogous to the computations before, we calculated for every B-scan the thicknesses $\text{CHL}_k = 1\,\text{mm}^{-1} \int_{(r_{\text{left}} - 1\,\text{mm})}^{r_{\text{left}}} |\text{RPE}_k(s_1) - \text{OCB}_k(s_1)| \text{d}s_1$ (left 1-mm region) and $\text{CHR}_k = 1\ \text{mm}^{-1} \int_{r_{\text{right}}}^{(r_{\text{right}} + 1\ \text{mm})} |\text{RPE}_k(s_1) - \text{OCB}_k(s_1)| \text{d}s_1$ (right 1-mm region), $1 \leqslant k \leqslant 5$, and tabulate for every B-scan the mean

$$\text{CHL}_m = \sum_{k=1}^{5} \text{CHL}_k / 5 \tag{25}$$

and the standard deviation

$$\text{CHL}_\sigma = \sqrt{\sum_{k=1}^{5} \text{CHL}_k^2 / 5 - \text{CHL}_m^2} \tag{26}$$

of the manually generated data, the automated measurement CHL_a and the error

$$\text{CHL-}\Delta_a^m = \text{CHL}_m - \text{CHL}_a \tag{27}$$

for the left 1-mm region (columns 1 to 4) as well as the respective values

Table 4 Choroid thickness, central foveal region. Entries defined in Eqs. (9), (21)–(24). Automated measurements in boldface.

No.	CHC_1 (μm)	CHC_2 (μm)	CHC_3 (μm)	CHC_4 (μm)	CHC_5 (μm)	CHC_m (μm)	CHC_σ (μm)	CHC_a (μm)	CHC-Δ_a^m (μm)
01	271.66	331.75	313.44	343.43	333.92	318.84	28.52	**331.24**	+12.40
02	223.16	275.73	247.20	248.41	252.62	249.42	18.70	**244.67**	−4.76
03	254.72	337.20	215.78	252.41	335.66	279.15	54.52	**296.98**	+17.83
04	242.13	251.76	238.70	244.24	246.88	244.74	4.93	**241.58**	−3.16
05	226.37	347.25	291.86	304.31	319.49	297.86	44.99	**286.36**	−11.49
06	187.51	411.10	159.64	341.58	377.51	295.47	114.38	**349.09**	+53.62
07	114.86	422.65	281.38	256.99	427.12	300.60	130.07	**268.10**	−32.49
08	201.90	306.79	257.06	263.82	282.00	262.31	38.88	**279.93**	+17.62
09	227.26	435.86	182.84	418.92	426.42	338.26	122.76	**269.98**	−68.28
10	182.24	381.53	228.73	365.97	323.49	296.39	87.22	**292.84**	−3.55
11	272.22	313.79	300.70	256.31	338.53	296.31	32.74	**263.54**	−32.77
12	192.36	256.46	226.16	209.99	258.15	228.62	28.79	**217.50**	−11.13
13	258.35	310.53	270.88	188.70	281.65	262.02	45.29	**206.06**	−55.97
14	170.42	425.76	184.30	390.76	288.36	291.92	116.23	**358.09**	+66.17
15	264.81	358.89	276.61	271.23	277.30	289.77	38.96	**285.84**	−3.93
16	289.13	333.78	305.76	302.68	313.38	308.94	16.42	**283.20**	−25.75
17	301.88	340.21	300.22	333.84	321.43	319.52	18.17	**308.64**	−10.88
18	242.53	431.37	148.44	410.13	429.63	332.42	129.62	**308.80**	−23.63
19	262.91	449.52	320.74	341.12	317.73	338.41	68.54	**259.98**	−78.43
20	167.76	445.10	117.06	336.65	333.96	280.10	134.65	**337.06**	+56.96
21	145.01	374.34	284.18	351.42	309.84	292.96	89.85	**310.74**	+17.78
22	225.88	269.18	219.13	254.01	269.21	247.48	23.75	**256.53**	+9.04
23	130.29	261.19	235.14	189.36	249.95	213.19	53.80	**223.09**	+9.91
24	243.19	361.64	345.57	313.90	331.10	319.08	45.94	**338.59**	+19.51
25	111.83	260.57	232.96	191.41	233.09	205.97	58.14	**218.02**	+12.05
26	184.50	300.73	203.39	204.72	304.32	239.53	58.07	**308.51**	+68.98
27	212.66	234.48	211.51	218.25	232.00	221.78	10.80	**225.02**	+3.24
28	320.39	345.20	317.12	331.04	339.61	330.67	12.05	**307.74**	−22.94
29	202.22	399.12	388.81	344.15	354.79	337.82	79.18	**347.94**	+10.13
30	327.02	396.14	360.28	367.17	356.15	361.35	24.75	**354.43**	−6.92
31	212.20	296.94	226.26	203.99	305.62	249.00	48.48	**221.38**	−27.62
32	279.22	337.76	272.18	238.91	330.26	291.67	41.63	**238.44**	−53.22
33	280.81	343.51	302.98	325.71	310.09	312.62	23.65	**317.77**	+5.14
34	241.16	302.84	260.70	256.64	268.72	266.01	22.90	**239.88**	−26.13

Table 4 (*Continued*).

No.	CHC_1 (μm)	CHC_2 (μm)	CHC_3 (μm)	CHC_4 (μm)	CHC_5 (μm)	CHC_m (μm)	CHC_σ (μm)	CHC_a (μm)	CHC-Δ_a^m (μm)
35	191.45	415.43	198.20	391.28	494.07	338.09	136.21	**349.30**	+11.21
36	183.46	458.92	223.92	262.12	263.85	278.45	106.12	**256.07**	−22.38
37	277.90	435.42	226.32	382.72	371.28	338.73	84.68	**246.68**	−92.05
38	156.89	419.53	278.60	340.28	354.34	309.93	99.13	**326.52**	+16.59
39	204.32	409.86	277.38	271.22	322.22	297.00	75.85	**326.97**	+29.97
40	266.49	310.92	248.97	251.99	270.77	269.83	24.77	**266.82**	−3.00
41	159.95	222.21	187.30	187.54	206.74	192.75	23.43	**196.77**	+4.02
42	205.60	241.47	216.52	212.71	246.27	224.51	18.18	**220.73**	−3.78
43	191.02	370.44	212.49	262.43	273.60	262.00	69.61	**285.08**	+23.09
44	248.58	379.83	238.63	251.50	348.34	293.38	65.67	**261.72**	−31.65
45	213.70	237.50	222.00	213.39	252.47	227.81	16.90	**223.84**	−3.98
46	247.65	303.36	245.30	209.12	291.61	259.40	38.19	**291.51**	+32.11
47	259.30	394.68	329.98	417.23	431.70	366.58	71.49	**281.47**	−85.11
48	253.16	281.77	259.68	236.20	302.03	266.57	25.68	**268.40**	+1.83
49	223.28	239.92	224.92	219.42	248.35	231.18	12.36	**228.34**	−2.84
50	320.77	361.43	271.60	211.14	344.36	301.86	60.95	**336.76**	+34.90

Table 5 Choroid thickness, left and right outer 1 mm regions. Entries defined in Eqs. (8), (10), (25)–(30). Automated measurements in boldface.

No.	CHL_m (μm)	CHL_σ (μm)	CHL_a (μm)	CHL-Δ_a^m (μm)	CHR_m (μm)	CHR_σ (μm)	CHR_a (μm)	CHR-Δ_a^m (μm)
01	300.61	17.99	**303.95**	+3.34	266.41	19.41	**285.45**	+19.05
02	253.43	18.28	**256.43**	+3.01	214.14	24.44	**205.03**	−9.11
03	261.66	25.17	**271.87**	+10.21	249.41	44.09	**218.54**	−30.87
04	188.23	9.82	**181.59**	−6.64	229.24	11.28	**216.64**	−12.60
05	292.18	54.68	**253.24**	−38.95	277.47	8.31	**271.45**	−6.02
06	279.61	120.04	**354.39**	+74.78	284.88	107.60	**357.03**	+72.15
07	250.15	80.70	**245.95**	−4.19	285.99	115.37	**287.25**	+1.26
08	266.23	48.98	**307.37**	+41.14	204.78	55.43	**171.77**	−33.01
09	281.46	99.73	**339.02**	+57.56	249.37	69.90	**305.08**	+55.71
10	297.38	87.68	**325.13**	+27.75	208.47	52.15	**189.29**	−19.18
11	301.92	35.39	**273.66**	−28.26	299.79	53.95	**286.14**	−13.65
12	260.25	39.37	**202.76**	−57.49	164.47	13.83	**155.58**	−8.89
13	204.89	16.86	**194.06**	−10.83	216.75	14.12	**208.25**	−8.50
14	257.72	85.74	**335.03**	+77.31	232.05	69.70	**347.08**	+115.03

Table 5 (*Continued*).

No.	CHL_m (μm)	CHL_σ (μm)	CHL_a (μm)	CHL-Δ_a^m (μm)	CHR_m (μm)	CHR_σ (μm)	CHR_a (μm)	CHR-Δ_a^m (μm)
15	328.26	35.91	**350.52**	+22.25	231.45	16.62	**234.71**	+3.26
16	307.84	17.61	**301.15**	−6.69	257.74	16.22	**253.29**	−4.45
17	327.04	22.29	**335.51**	+8.47	241.81	16.53	**240.60**	−1.21
18	317.40	103.81	**216.28**	−101.12	340.44	104.91	**341.92**	+1.48
19	328.71	63.42	**341.42**	+12.70	310.92	57.82	**317.31**	+6.38
20	299.66	141.91	**321.68**	+22.02	220.05	45.80	**253.85**	+33.79
21	279.86	126.00	**255.59**	−24.27	258.12	51.69	**294.39**	+36.26
22	246.12	52.54	**271.77**	+25.65	232.73	9.55	**239.16**	+6.43
23	198.05	31.79	**183.90**	−14.15	192.41	29.16	**165.61**	−26.79
24	259.65	60.13	**278.75**	+19.10	254.78	45.79	**261.67**	+6.89
25	213.28	56.65	**241.16**	+27.87	218.43	52.18	**235.20**	+16.76
26	268.17	52.37	**234.48**	−33.70	244.86	37.30	**309.68**	+64.82
27	263.69	9.25	**262.89**	−0.80	193.55	4.94	**205.86**	+12.32
28	344.73	7.54	**347.59**	+2.85	268.96	17.60	**257.52**	−11.44
29	301.14	47.38	**324.37**	+23.23	253.46	60.77	**263.65**	+10.20
30	342.00	7.60	**342.56**	+0.57	334.02	23.42	**332.53**	−1.50
31	283.61	64.26	**205.12**	−78.49	193.06	20.87	**175.81**	−17.24
32	261.93	33.22	**291.62**	+29.69	244.99	24.66	**256.26**	+11.27
33	237.47	33.25	**264.12**	+26.64	333.10	8.50	**343.81**	+10.70
34	296.47	23.35	**276.34**	−20.13	197.33	12.20	**179.65**	−17.68
35	318.13	121.27	**343.11**	+24.98	331.04	123.78	**307.08**	−23.95
36	234.34	86.74	**338.18**	+103.85	279.65	63.73	**295.51**	+15.87
37	289.01	89.35	**281.85**	−7.15	264.74	33.85	**267.64**	+2.90
38	261.53	55.36	**269.86**	+8.32	308.34	87.67	**330.20**	+21.86
39	293.36	32.60	**309.27**	+15.91	262.18	68.89	**230.46**	−31.73
40	248.17	32.55	**275.41**	+27.24	266.88	18.58	**292.51**	+25.64
41	151.86	25.77	**154.03**	+2.17	150.26	21.33	**155.44**	+5.18
42	253.80	8.76	**251.59**	−2.21	157.77	23.69	**151.94**	−5.82
43	262.58	42.93	**278.71**	+16.13	300.89	52.37	**346.90**	+46.00
44	244.85	92.10	**185.68**	−59.17	259.21	58.94	**256.60**	−2.61
45	232.03	26.03	**227.40**	−4.63	195.37	15.31	**185.58**	−9.79
46	311.19	25.08	**333.42**	+22.22	210.41	19.03	**227.90**	+17.48
47	340.00	66.17	**273.79**	−66.22	344.78	42.11	**318.65**	−26.13
48	260.05	29.08	**257.52**	−2.53	237.79	23.07	**255.58**	+17.78
49	260.30	8.64	**262.78**	+2.48	166.71	12.90	**169.78**	+3.07
50	279.30	62.56	**248.46**	−30.84	287.61	35.74	**255.27**	−32.34

Table 6 Properties of OCT data used in the cited references.

Reference	Imag. method	Device	Averaging	(Semi-)manual OCB segm.	Automated OCB segm.
Manjunath et al.[4]	SD-OCT	Carl Zeiss Meditec, Cirrus HD-OCT	20	•	
Manjunath et al.[7]	SD-OCT	Carl Zeiss Meditec, Cirrus HD-OCT	20	•	
Hu et al.[39]	SD-OCT	Heidelberg, Spectralis	9		•
Zhang et al.[41]	SD-OCT	Carl Zeiss Meditec, Cirrus HD-OCT	none		•
Zhang et al.[42]	SD-OCT	Topcon, 3D-OCT 1000 / Topcon, 3D-OCT 2000	none		•
Present study	**SD-OCT**	**Heidelberg, Spectralis**	**10**		•
Cho et al.[23]	EDI SD-OCT	Heidelberg, Spectralis	100	•	
Dhoot et al.[6]	EDI SD-OCT	Heidelberg, Spectralis	100	•	
Ding et al.[24]	EDI SD-OCT	Heidelberg, Spectralis	100	•	
Flores-Moreno et al.[27]	EDI SD-OCT	Topcon, 3D-OCT 2000	50	•	
Ikuno et al.[28]	EDI SD-OCT	Heidelberg, Spectralis	100	•	
Li et al.[29]	EDI SD-OCT	Heidelberg, Spectralis	25	•	
Li et al.[30]	EDI SD-OCT	Heidelberg, Spectralis	25	•	
Li et al.[9]	EDI SD-OCT	Heidelberg, Spectralis	?	•	
Lindner et al.[31]	EDI SD-OCT	Heidelberg, Spectralis	100	•	
Margolis and Spaide[32]	EDI SD-OCT	Heidelberg, Spectralis	100	•	
Matsuo et al.[37]	EDI SD-OCT	Heidelberg, Spectralis	100	•	
Matsuo et al.[37]	EDI SD-OCT	Topcon, 3D-OCT 1000	50	•	
Read et al.[5]	EDI SD-OCT	Optopol, Copernicus SOCT-HR	?	•	
Shin et al.[34]	EDI SD-OCT	Topcon, 3D-OCT 2000	8	•	
Sim et al.[35]	EDI SD-OCT	Heidelberg, Spectralis	?	•	
Alonso-Caneiro et al.[38]	EDI SD-OCT	Heidelberg, Spectralis	30		•
Lee et al.[36]	EDI SD-OCT	Carl Zeiss Meditec, Cirrus HD-OCT	20		•
Tian et al.[40]	EDI SD-OCT	Heidelberg, Spectralis	?		•
Esmaeelpour et al.[25]	SS-OCT	3D 1060 nm-OCT	?	•	
Esmaeelpour et al.[26]	SS-OCT	3D 1060 nm-OCT	?	•	
Hirata et al.[12]	SS-OCT	Topcon, SS-OCT	?	•	
Ikuno et al.[28]	SS-OCT	1060 nm-OCT	?	•	
Matsuo et al.[37]	SS-OCT	Atlantis, DRI OCT-1	96	•	
Ruiz-Moreno et al.[33]	SS-OCT	Topcon, SS-OCT	96	•	
Usui et al.[8]	SS-OCT	Topcon, SS-OCT	32	•	
Kajić et al.[43]	SS-OCT	3D 1060 nm-OCT	?		•
Zhang et al.[42]	SS-OCT	Topcon, SS-OCT	?		•
Torzicky et al.[13]	PS-OCT	1040 nm-OCT	?		•

$$\mathrm{CHR}_m = \sum_{k=1}^{5} \mathrm{CHR}_k/5, \tag{28}$$

$$\mathrm{CHR}_\sigma = \sqrt{\sum_{k=1}^{5} \mathrm{CHR}_k^2/5 - \mathrm{CHR}_m^2}, \tag{29}$$

the automated measurement CHR_a and the error

$$\mathrm{CHR}\text{-}\Delta_a^m = \mathrm{CHR}_m - \mathrm{CHR}_a \tag{30}$$

for the right 1-mm region (columns 5 to 8).

3.3 *Discussion of the Results*

General comparison with other methods from the literature. When comparing different methods for OCB segmentation and choroidal thickness measurement, a basic methodical problem is caused by the large variation of quality of the underlying image data [Ref. 36, p. 2869]. The majority of the existing studies is based on data generated by special imaging modes and/or high line averaging (see Table 6). Another problem addressed in the literature is the repeatability of the measurements, which extends to the applied segmentation methods.

In general, manual delineation of the OCB, even with assistance of built-in software (calipers), must cope with serious difficulties as wide intra- and inter-observer variability and large time effort (cf. Ref. 28, p. 5539; Ref. 37, p. 7635). The crucial point, however, is the required quality of the underlying OCT data. Table 6 shows that, for manual OCB segmentation, highly averaged data are widely preferred. The results of the present study confirm these observations, showing a considerable variation in the five manual delineations. Thus, for moderately averaged SD-OCT data, a stable automated method as the proposed one seems to be clearly preferable to manual segmentation.

For an exemplary comparison with graph-theoretical or statistical automated segmentation methods, we choose the papers 38, 39, and 43 (the setting of Ref. 39 is closest to the present study). By overall inspection, our approach leads to results that are fairly well comparable with the aforementioned studies, even though Refs. 38 and 43 used data generated by special imaging modules, containing a considerably lower amount of noise. The errors in OCB segmentation and choroidal thickness measurement obtained in Refs. 38 and 39 fit into the same range as the ones obtained in the present study. A detailed quantitative comparison with the results from Ref. 43 is not possible due to the different error measure used there. Since their method involves model parameters generated from the examination of a training set, it is unclear whether the measurements are externally repeatable. Furthermore, for this and the method from Ref. 38, it may be questioned what constitutes the lower bound of image quality limiting their application. For graph-theoretical methods, a general challenge is to decide whether the possible occurrence of long-range correlations influences local statistics.

Comparison of manual and automated ILM/RPE boundary segmentation. In order to demonstrate its reliability, the quadratic measure filter method has been applied purposefully even to the "simple" detection of the ILM and RPE/choroid boundaries. In Table 7, the information from Table 2 is summarized, showing for every column the mean and the standard deviation of its 50 entries.

More precisely, we find that $\overline{\mathrm{ILM}}\text{-}|\Delta|_a^m$ and $\overline{\mathrm{ILM}}\text{-}\Delta_a^m$ are less than 1 px (3.87 μm) for 45 of the 50 and 50 of the 50 investigated scans, respectively. Further, $\overline{\mathrm{RPE}}\text{-}|\Delta|_a^m$ is less than 2 px for 34 of the 50 and less than 3 px for 45 of the 50 scans while $\overline{\mathrm{RPE}}\text{-}\Delta_a^m$ is less than 2 px for 38 of the 50 and less than 3 px for 45 of the 50 scans. The accuracy of these results is comparable with the mean absolute errors mentioned in the literature, e.g., Ref. 18, p. 52, Fig. 22 C (ILM boundary: 4 μm, RPE boundary: 3.6 μm, automated detection versus mean of three manual delineations), Ref. 21, p. 1752, Table 1, third column (ILM boundary: 2.7 μm, RPE boundary: 4.2 μm, automated detection versus single manual delineation) and Ref. 38, p. 2809, Table 1 (RPE boundary: 3.09 μm/3.23 μm in two samples, automated detection versus single manual delineation). Our results are of the same magnitude for the ILM boundary and slightly larger for the RPE/choroid boundary. For the latter, the mean absolute error reduces to 6.26 ± 2.42 μm and the mean error to -3.27 ± 4.93 μm when the five outliers (Table 2, lines 9, 11, 15, 18, and 32) are excluded. We therefore summarize that the reliability of the quadratic measure filter method is well confirmed by our results.

Comparison of manual and automated OCB segmentation. As mentioned above, the manual delineation of OCB shows high variability between the five graders; see Table 3. The data sample contains a number of scans showing the OCB with a very weak contrast, leading to considerable disagreement between the manual segmentations. In the following Table 8, the information from Table 3 is summarized, showing the mean and the standard deviation of its 50 entries for columns 1 to 4.

Our automated OCB determination satisfies $\overline{\mathrm{OCB}}\text{-}|\Delta|_a^m \leqslant \overline{\mathrm{OCB}}_\sigma$ for 38 of the 50 investigated scans. The reliability of the method is shown as well by the fact that the inclusion

Table 8 Summary: results of automated OCB detection. Quantities defined as in Table 3.

	$\overline{\mathrm{OCB}}_\sigma$ (μm)	$\overline{\mathrm{OCB}}\text{-}\lvert\Delta\rvert_a^m$ (μm)	$\overline{\mathrm{OCB}}\text{-}\Delta_a^m$ (μm)	Perc. (%)
Mean of the entries from Table 3	43.67	35.76	−7.68	83.3
Std. dev. of the entries from Table 3	(n/a)	±27.32	±29.36	±10.0

Table 7 Summary: results of automated ILM and RPE detection. Quantities defined as in Table 2.

	$\overline{\mathrm{ILM}}_\sigma$ (μm)	$\overline{\mathrm{ILM}}\text{-}\lvert\Delta\rvert_a^m$ (μm)	$\overline{\mathrm{ILM}}\text{-}\Delta_a^m$ (μm)	$\overline{\mathrm{RPE}}_\sigma$ (μm)	$\overline{\mathrm{RPE}}\text{-}\lvert\Delta\rvert_a^m$ (μm)	$\overline{\mathrm{RPE}}\text{-}\Delta_a^m$ (μm)
Mean of the entries from Table 2	2.91	3.24	−0.08	3.24	7.16	−4.45
Std. dev. of the entries Table 2	(n/a)	±0.48	±1.00	(n/a)	±3.61	±5.93

Table 9 Summary: choroidal thickness, central foveal region. Quantities defined as in Table 4. Automated measurements in boldface.

	CHC_m (μm)	CHC_σ (μm)	CHC_a (μm)	CHC-Δ_a^m (μm)	|CHC-Δ_a^m| (μm)
Mean of the entries from Table 4	283.56	55.93	**279.29**	−4.27	25.64
Std. dev. of the entries from Table 4	±41.81	(n/a)	±44.73	±34.71	±24.02

Table 11 Summary: choroidal thickness, right outer 1 mm region. Quantities defined as in Table 5. Automated measurements in boldface.

	CHR_m (μm)	CHR_σ (μm)	CHR_a (μm)	CHR-Δ_a^m (μm)	|CHR-Δ_a^m| (μm)
Mean of the entries from Table 5	248.58	40.34	**254.28**	+5.70	19.88
Std. dev. of the entries from Table 5	±48.73	(n/a)	±**58.00**	±28.28	±21.11

$\mathrm{Min}_{1\leqslant k\leqslant 5}\mathrm{OCB}_k(s_1)\leqslant \mathrm{OCB}_a(s_1)\leqslant \mathrm{Max}_{1\leqslant k\leqslant 5}\mathrm{OCB}_k(s_1)$ is satisfied on more than 75% of the interval length for 41 of the 50 scans. In Ref. 39, analyzing data with a comparable amount of noise, a mean absolute error of 27.23 ± 7.43 μm and a mean error of -2.05 ± 12.59 μm were obtained (ibid., p. 1724, Table 2, automated detection versus consensus of two manual delineations). In Ref. 38, using EDI SD-OCT data with higher averaging, mean absolute errors of 12.72 ± 7.28 μm and 16.53 ± 11.34 μm and mean errors of 3.65 ± 10.68 μm and 0.01 ± 15.58 μm were documented (ibid., p. 2809, Table 1, two samples, automated detection versus single manual delineation). Our values, as summarized in Table 8, are slightly larger.

Comparison of manual and automated choroidal thickness measurements. The results from Tables 4 and 5 are summarized in the following Tables 9–11. More precisely, the first four columns of Table 9 contain the mean and the standard deviation of the 50 entries from Table 4, columns 6 to 9. In column 5, we appended mean and standard deviation of the absolute values of the entries from Table 4, column 9. Analogously, the first four columns of Tables 10 and 11 display the mean and the standard deviation of the 50 entries from Table 5, columns 1 to 4 and 5 to 8, respectively. In addition, we show the mean and standard deviation of the absolute values of the errors from Table 5, columns 4 and 8, respectively.

Again, the outcomes of the automated procedure fit excellently into the standard deviation intervals of the values generated from the manual delineations. For the central foveal region, we find $|\mathrm{CHC}\text{-}\Delta_a^m| \leqslant 1.25 \cdot \mathrm{CHC}_\sigma$ for 46 of the 50 investigated scans; for the left 1-mm region, we have $|\mathrm{CHL}\text{-}\Delta_a^m| \leqslant 1.0 \cdot \mathrm{CHL}_\sigma$ for 46 of the 50 scans, and for the right 1-mm region, we get $|\mathrm{CHR}\text{-}\Delta_a^m| \leqslant 1.0 \cdot \mathrm{CHR}_\sigma$ for 44 of the 50 scans.

The errors observed in Tables 9–11 compete fairly well with Refs. 38 and 39, who averaged choroidal thickness measurements over the full length of the B-scans. Reference 38 obtained mean absolute errors of 12.96 ± 9.00 μm and 16.27 ± 11.48 μm and mean errors of -1.01 ± 12.43 μm and 2.35 ± 15.48 μm (ibid., p. 2810, Table 2, two samples, automated detection versus single manual delineation) while Ref. 39 found a mean error of 0.12 ± 14.12 μm (ibid., p. 1724, Table 2, automated detection versus consensus of two manual delineations). The agreement between manual and automated choroidal thickness measurements for the central foveal region is visualized by Bland–Altman plots;[65–67] see Fig. 4. The shown examples are based on Table 4 (central foveal region). The agreement between the mean of the observers and the automated method is excellent. The five plots of automated versus single manual thickness measurements confirm considerable inter-observer variation when measuring the same subjects. Nevertheless, the automated method fits well into the 95% boundaries in all cases. Once more it becomes clear that, for data with the given image quality, the automated method is superior to a single manual determination.

Table 10 Summary: choroidal thickness, left outer 1 mm region. Quantities defined as in Table 5. Automated measurements in boldface.

	CHL_m (μm)	CHL_σ (μm)	CHL_a (μm)	CHL-Δ_a^m (μm)	|CHL-Δ_a^m| (μm)
Mean of the entries from Table 5	272.83	50.71	**275.65**	+2.82	26.76
Std. dev. of the entries from Table 5	±40.62	(n/a)	±**51.45**	±37.13	±26.16

Discussion of the obtained thickness values. Although not the focus of the present study, the obtained thickness measurements will be briefly set in position. The automatically derived choroidal thicknesses within our study are in line with previously obtained results from the literature; see Ref. 5, p. 3589, Table 1, column 1 (mean of eight foveal locations, 326 ± 64 μm, children of ages 4 to 12), Ref. 29 p. 552, Table 1 (central foveal region, 348 ± 72.1 μm, boys of ages 11 to 12 and 369 ± 80.8 μm, girls of ages 11 to 12), Ref. 30, p. 621, Table 3 (macular region, 288 ± 59 μm, 328 ± 55 μm, and 309 ± 52 μm, three groups of children of ages 11 to 12) and, Ref. 33, p. 353 (macular region, 285.2 ± 56.7 μm, children of ages 3 to 18). Exemplarily, we add a plot displaying the relation between the choroidal thicknesses for the central foveal region and the axial length (Fig. 5), which shows a clustering of boys and girls analogously to Ref. 29, p. 553, Fig. 1. Due to the small number of probands, we refrain from claiming other trends from this illustration. In a forthcoming study, we plan to analyze a larger sample from the LIFE cohort study.

3.4 *Limitations of the Proposed Method; Possible Errors*

Methodological limitations and possible errors. Within the proposed algorithm, there are at least two possible sources of systematic errors. First, choroidal thickness is measured in the vertical direction within the scan instead of the (geometrically) normal direction to the obtained RPE boundary, thus neglecting the curvature of the layer boundary. Second, Eq. (7) involved in the determination of the left and right 1-mm measurement regions is based on a model eye of an adult instead of a child.

Automated layer detection may produce errors, which a human observer would avoid. In rare cases, the feature recognition routine involved in the detection of the RPE boundary

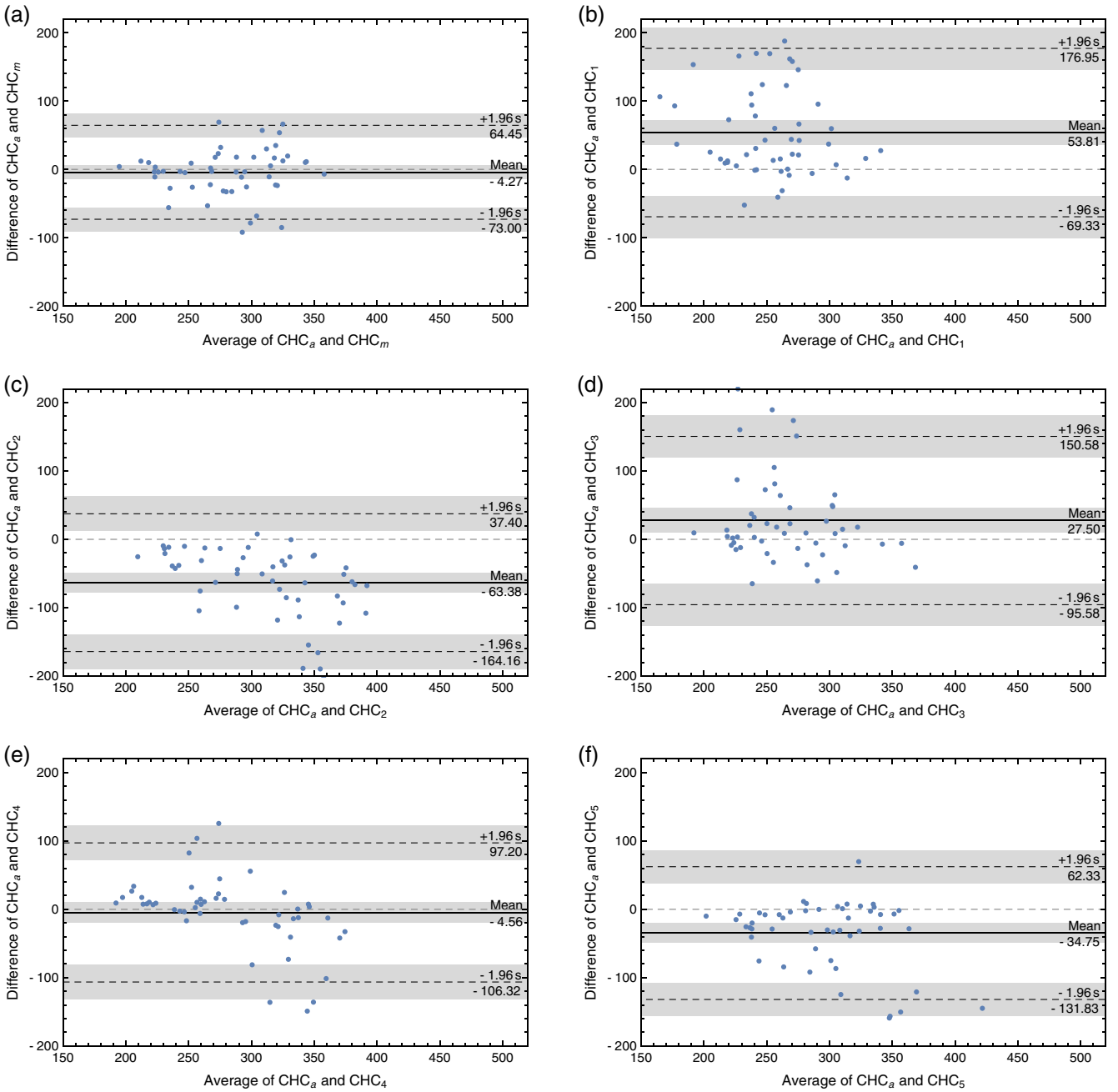

Fig. 4 Bland–Altman plots for the choroidal thickness measurements, central foveal region. Values of CHC_a, CHC_m, and CHC_k, $1 \leqslant k \leqslant 5$, are taken from Table 4. Black dashed lines depict the mean difference between automated and manual delineation and the 95% limits of agreement (LOA). Ninety-five percent confidence intervals for the mean and the LOA are plotted in gray. p-values indicate the statistical significance of deviation of the mean from zero. (a) $(CHC_a + CHC_m)/2$ versus $(CHC_a - CHC_m)$, $p = 0.5821$. (b) $(CHC_a + CHC_1)/2$ versus $(CHC_a - CHC_1)$, $p = 0.0000$. (c) $(CHC_a + CHC_2)/2$ versus $(CHC_a - CHC_2)$, $p = 0.0000$. (d) $(CHC_a + CHC_3)/2$ versus $(CHC_a - CHC_3)$, $p = 0.0091$. (e) $(CHC_a + CHC_4)/2$ versus $(CHC_a - CHC_4)$, $p = 0.9154$. (f) $(CHC_a + CHC_5)/2$ versus $(CHC_a - CHC_5)$, $p = 0.0000$.

misidentifies parts of the next hyperreflective layer above the RPE for the RPE boundary itself, thus overestimating the resulting choroidal thickness (this error accounts for the outliers of $\overline{\text{RPE}}$-$|\Delta|_a^m$ and $\overline{\text{RPE}}$-Δ_a^m in Table 2, lines 9, 11, 15, 18, and 32). If druses were present (not occurring in the studied sample), similar errors would be possible.

The line averaging of 10 used in the study constitutes a lower bound for the applicability of the method, which becomes infeasible for data corrupted with stronger noise. It is to be expected that for older adult subjects, more averaging is required due to naturally occurring opacifications in the visual pathway.

Limitations due to choroid physiology. As mentioned in the introduction, choroidal thickness can be short-term modulated, even following a diurnal rhythm. As the prevailing part of the literature, the present study is unable to discern such effects when performing single OCT measurements.

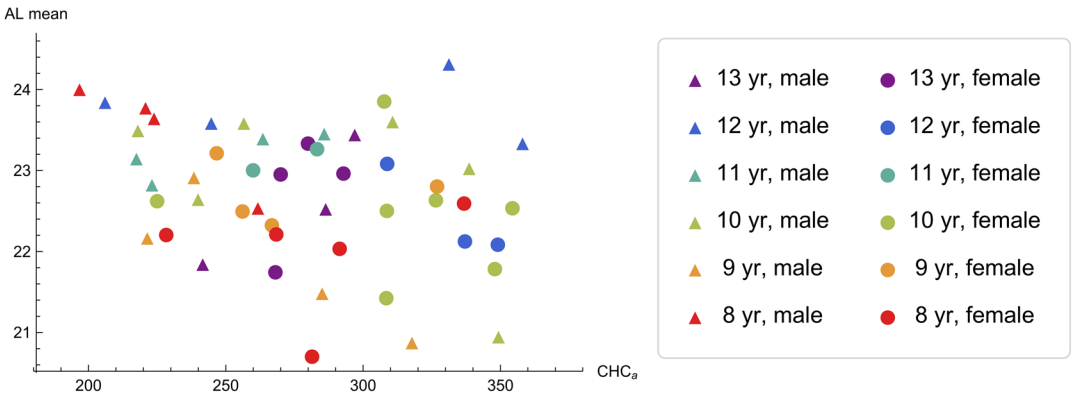

Fig. 5 Mean choroidal thickness (central foveal region) from automated method plotted versus axial length. CHC$_a$ thickness values (in μm) from Table 4, mean axial length (in mm) from Table 1.

Observed structure of the OCB compared with histology. In difference to Refs. 36 and 38 as well as to most studies performing manual OCB delineation, we observed a relatively bumpy structure of the OCB in most of our automated segmentations [the result shown in Fig. 1(b) is typical]. In the following, we will shortly discuss whether our observations correspond to the histological composition of the suprachoroid and choroid/sclera border.

Note first that, in the case of manual segmentation, the OCB is usually fixed by marking a comparatively small number of measurement points [see, e.g., Ref. 4, p. 326, Fig. 1 (11 points), Ref. 24, p. 9556, Fig. 1 (9 points), Ref. 28, p. 5537, Fig. 1 (6 points), and Ref. 31, p. 876 (25 points per volume scan)] and possible subsequent spline interpolation. Necessarily, boundary lines resp. thickness maps resulting from such procedures appear very smooth. In contrast, there are several studies with automated segmentation reporting a bumpy structure of the OCB [we mention Ref. 13, p. 7570, Fig. 2, Ref. 42, p. 3204, Fig. 4(d), and Ref. 43, p. 99, Fig. 5(b)].

Histological investigation of the human suprachoroid shows an irregular distribution of features with low and high reflectance in visible light (melanocytes resp. translucent parts and collagen fibers) throughout this transition layer [Fig. 6(a)]. Cross-section reveals a sharply defined histological border between the suprachoroid and the collagen bundles of the sclera which, however, does not necessarily correspond to an optically

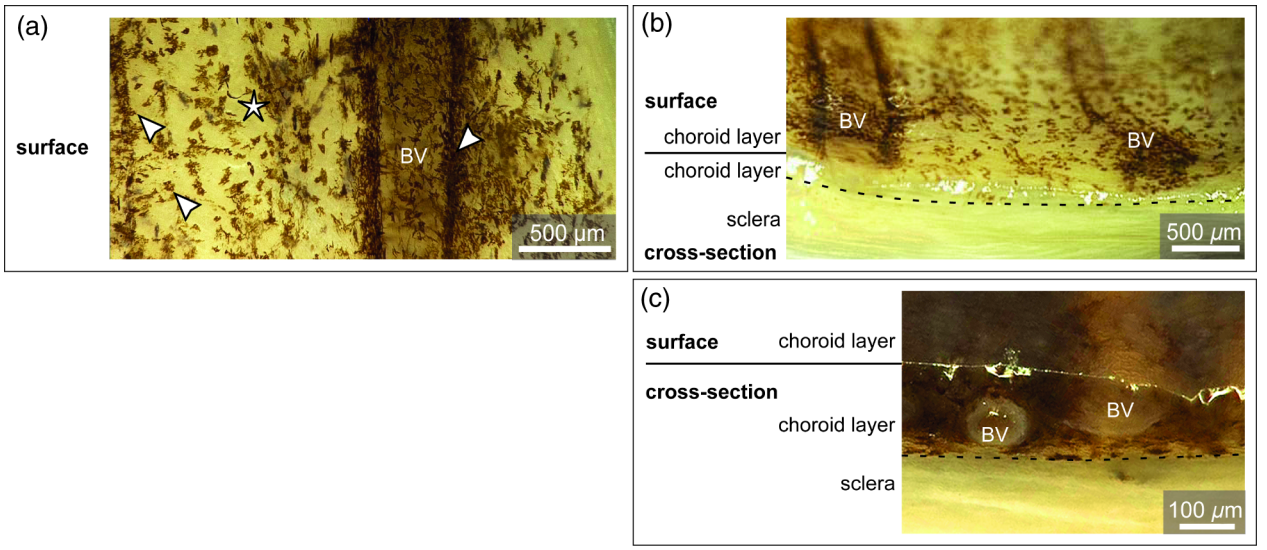

Fig. 6 Fixed unstained histological preparations/sections of the human choroid-sclera interface. (a) Image shows a plane view onto the outer parts of the choroid/suprachoroid and the inner part of the sclera (most parts of choroidal stroma removed). Branched light-absorbing melanocytes (arrowheads) are irregularly distributed in the suprachoroid and surround large blood vessels (BV). The sclera appears as bright, highly reflecting tissue (star) through the translucent components of the choroid between the light-absorbing elements. (b) View onto the edge of a frontal cross-section of the choroid/sclera interface combined with a plane view onto the surface of the outer choroid with collapsed blood vessels [same region as in (a)]. The cross-section nicely reveals the translucent gel-like structure of the remaining stroma and the suprachoroid and the (birefringent) brightly reflecting optical properties of the collagen bundles of the sclera. Suprachoroid/sclera interface marked by the dotted line. (c) Cross-section of the choroid/sclera interface with large blood vessels [region different from (a) and (b) at higher magnification, choroidal stroma still present]. The histological border of the suprachoroid/sclera interface (dotted line) appears to be very tight, smooth, and clearly identifiable.

distinguishable brightness jump [absent in Fig. 6(b), present in Fig. 6(c)]. Therefore, it is likely that the histological border may not be represented as a separate reflectivity feature within the OCT data. Consequently, our method provides a highly reliable inner approximation of the histologically determined choroid boundary but possibly underestimates the choroidal thickness. If so, the same would be true for the vast majority of thickness measurements presented in the literature. In view of Fig. 6(a), the bumpy appearance of the detected OCB may well correspond to the scattered distribution of suprachoroidal tissue regions with sufficiently high concentration of melanocytes.

4 Conclusions

A novel method for the automated detection of the OCB within SD-OCT image data based on an image model within the space of BV functions and the application of quadratic measure filters was established and proved to be reliable. Additionally, the method was successfully applied to the automated segmentation of the ILM and RPE/choroid boundaries. A particular advantage of the presented approach is its capability of dealing with data generated without special imaging modules and moderate averaging only. For such data, as available in the LIFE Child and LIFE Adult cohort studies, the method is clearly preferable to manual OCB segmentations and subsequent thickness derivations. The presented algorithms can be externally repeated independent of the sample used in the study.

Disclosures

The authors declare that they have no competing interests.

Appendix: Mathematical Background

A.1 Edge Detection within Noisy Grayscale Images

Our approach fits into a mathematical framework where a grayscale image containing the reflectivity information is understood as a function $x(s):Q\to\mathbb{R}$ rather than as a "discrete" entity. Then the acquisition of OCT data $I(s)$ can be modeled as

$$I(s)=\mathcal{S}[x(s)]\cdot\mathcal{N}(s), \tag{31}$$

where $x(s)$ represents the "ideal" reflectivity information, $\mathcal{S}$ is an operator encoding the acquisition process (also comprising the known systematic errors of the imaging device), and $\mathcal{N}(s)$ describes the noise, which enters in OCT images basically in a multiplicative way, cf. Ref. 68, p. 1208. Of course, the edge structure in $x(s)$ is distorted by the noise term as well. Consequently, the recognition of edges requires a partial removal of the noise at least.

In large parts of the literature, denoising is performed first by subjecting the data $I(s)$ to a suitable diffusion process (see Ref. 69, pp. 94 ff., for a closer mathematical analysis of diffusion-based image restoration), which is followed by separate, more or less sophisticated edge detection steps. In another largely pursued approach, the formal reconstruction of $x(s)=\mathcal{S}^{-1}[I(s)/\mathcal{N}(s)]$, which is unstable due to the presence of the noise term, is replaced by a regularized variational or optimal control problem in suitable function spaces. Often, the cost functionals are designed particularly for the suppression of speckle noise.[70–72] While solving such problems, a simultaneous edge detection is often possible, e.g., by use of Ambrosio–Tortorelli type functionals (see Ref. 69, p. 169 f.) or by incorporation of gradient constraints.[73]

A.2 Functions of Bounded Variation

In the present study, we model an OCT image as an integrable function $x:Q\to[0,1]$ of bounded variation (BV) defined on a rectangle $Q\subset\mathbb{R}^2$. A BV function x must satisfy the condition

$$\|Dx\|_{TV}=\sup\left\{\int_\Omega x(s)[\partial\psi_1(s)/\partial s_1+\partial\psi_2(s)/\partial s_2]\mathrm{d}s\,|\,\psi_1,\psi_2\right.$$
$$\left.\in C_0^1(Q),|\psi_1(s)|\leqslant 1,|\psi_2(s)|\leqslant 1\text{ for all }s\in Q\right\}<(+\infty), \tag{32}$$

(see Ref. 74, pp. 166 ff., for a rigorous mathematical treatment). The use of this function space in image processing has a long and successful tradition (see Ref. 75, pp. 174 ff.) since, on one hand, a notion of weak derivatives is available, and on the other hand, functions of BVs are allowed to have jumps. More precisely, the edge structure within the image x is defined as the union $S_x\subset Q$ of finitely many piecewise smooth curves, along which the function x admits jumps of the height $x^+(s)-x^-(s)$, $s\in S_x$. In the following, we will outline how this edge structure can be identified by the approach of quadratic measure filters.[45,47–49] From the methods described above, this approach differs in the fact that the smoothing kernel applied to the noisy data $I(s)$ forms an integral part of the edge detector itself.

A.3 Edge Detection by Quadratic Measure Filters

In mathematical terms, the weak partial derivative $D_{s_i}x=\mu'+\mu''+\mu'''$ of a BV function x can be identified with the sum of three signed measures μ', μ'', and μ''': the first one (which is absolutely continuous with respect to the 2-D Lebesgue measure $\mathcal{L}^2$) representing the usual partial derivative $\partial x/\partial s_i$ where it exists but measuring the jump set with zero, the second one encoding the position and height of possible jumps while the third part μ''' (the so-called Cantor part) can be neglected in medical image processing. Consequently, in order to identify the edge structure within x, one has to access the measure μ''. Indeed, this is possible by the following theorem yielding an (implicit) description of μ'' in terms of a limit relation for measures.

Theorem. (Ref. 48, p. 2, Theorem 1; cf. also Ref. 45, p. 701 f., Theorem 3.1.) We choose a nonnegative, symmetric kernel $\varphi\in C^\infty(\mathbb{R}^2)$, which is concentrated on the unit ball and normed by $\int_{\mathbf{R}^2}\varphi(s)\mathrm{d}s=1$. With the aid of φ, we build a family of smoothing kernels $\varphi_\varepsilon(s)=\varepsilon^{-2}\varphi(s/\varepsilon)$, $0<\varepsilon\leqslant 1$. Then for every integrable function $x:Q\to[0,1]$ of bounded variation, the following limit relation holds true:

$$\lim_{\varepsilon\to 0+0}\int_{\mathbf{R}^2}\psi(s)\cdot\varepsilon|\nabla(x*\varphi_\varepsilon)(s)|^2\mathrm{d}\mathcal{L}^2(s)$$
$$=C\int_{S_x}\psi(s)\cdot|x^+(s)-x^-(s)|^2\mathrm{d}\mathcal{H}^1(s) \tag{33}$$

for all test functions $\psi\in C^0(\mathbb{R}^2)$ with compact support. Here $\mathcal{L}^2$ and $\mathcal{H}^1$ denote the 2-D Lebesgue measure on $\mathbb{R}^2$ and the one-dimensional Hausdorff measure on the jump set $S_x\subset Q$ of the

function x, respectively. The constant $C > 0$ depends on the kernel φ only.

Since the limit in Eq. (33) is formed with respect to (weak*-) convergence in the space of signed measures, the assertion takes the form of a variational equation, which holds true for a whole set of test functions ψ. The integral on the left-hand side of Eq. (33) is termed a "quadratic measure filter" and can be understood as the approximation of a quantity, which is concentrated on the jump set of x and measures the square of the jump height. Note that the theorem remains true for the Gauss kernel and noncompactly supported test functions $\psi \in C^0(\mathbb{R}^2)$ as well, cf. Ref. 47.

Assuming that an admissible test function ψ is supported on a subset $\Omega \subset Q$, Eq. (33) implies the alternative

$$\lim_{\varepsilon \to 0+0} \int_\Omega \psi(s) \cdot \varepsilon |\nabla(x * \varphi_\varepsilon)(s)|^2 \mathrm{d}s = \begin{cases} C(x, \psi, \Omega) > 0 & \text{if } \mathcal{H}^1(\Omega \cap \mathrm{S}_x) > 0; \\ 0 & \text{if } \mathcal{H}^1(\Omega \cap \mathrm{S}_x) = 0. \end{cases} \tag{34}$$

From Eq. (34), the edge detectors from Sec. 2.3 are derived by insertion of a fixed test function ψ supported on Ω and subsequent discretization of the integral (here the function x is replaced by the pixeled data I). Then, instead of passing to the limit, one may inspect the local maxima of the resulting detectors for fixed $\varepsilon \in (0, 1]$ while moving the test function and its support through appropriate subsets of Q. Namely, the maxima search will be constrained to the intersection of the sets $\{s \in Q | \partial(I * \varphi_\varepsilon)(s)/\partial s_2 \geq 0\}$ or $\{s \in Q | \partial(I * \varphi_\varepsilon)(s)/\partial s_2 < 0\}$ with narrow vertical stripes, thus accounting for the mainly horizontal orientation of the layer structure within OCT data.

Acknowledgments

This publication is supported by LIFE Leipzig Research Center for Civilization Diseases, Leipzig University. LIFE is funded by means of the European Union, the European Social Fund (ESF), the European Regional Development Fund (ERDF) and the Free State of Saxony within the framework of the excellence initiative. The Integrated Research and Treatment Center Adiposity Diseases is funded by the German Federal Ministry of Education and Research (Grant No. 01EO1501). Marcus Wagner gratefully acknowledges support by the Max-Planck-Gesellschaft for granting a stay at the MPI for Mathematics in the Sciences, Leipzig, in 2015 and 2016. The authors would like to express their sincere thanks to Heike Lange (Leipzig University Hospital, Department of Ophthalmology/LIFE Leipzig Research Center for Civilization Diseases, Leipzig University) for carrying out the presented optical coherence tomography measurements as well as obtaining the axial length and corneal radii values employed and to Claudia Holzhey (Heidelberg Engineering GmbH, Heidelberg) for her support with the implementation of the measurement technique as part of the LIFE Child study. Furthermore, the authors would like to thank the following researchers for carrying out manual segmentations for this paper: Anna Xenia Bestehorn (Münster), Sophia Scheibe (Leipzig), and Anja Schirmer (Berlin).

References

1. D. L. Easty and J. M. Sparrow, Eds., *Oxford Textbook of Ophthalmology*, Vol. **1**, Sections 1–2.10, Oxford University Press, New York (1999).
2. D. L. Nickla and J. Wallman, "The multifunctional choroid," *Progress in Retinal and Eye Research* **29**, 144–168 (2010).
3. L. A. Remington, *Clinical Anatomy of the Visual System*, 2nd ed., Elsevier/Butterworth Heinemann, St. Louis (2005).
4. V. Manjunath et al., "Choroidal thickness in normal eyes measured using Cirrus HD optical coherence tomography," *Am. J. Ophthalmol.* **150**(3), 325–329 (2010).
5. S. A. Read et al., "Choroidal thickness in childhood," *Invest. Ophthalmol. Visual Sci.* **54**(5), 3586–3593 (2013).
6. D. S. Dhoot et al., "Evaluation of choroidal thickness in retinitis pigmentosa using enhanced depth imaging optical coherence tomography," *Br. J. Ophthalmol.* **97**(1), 66–69 (2013).
7. V. Manjunath et al., "Analysis of choroidal thickness in age-related macular degeneration using spectral-domain optical coherence tomography," *Am. J. Ophthalmol.* **152**(4), 663–668 (2011).
8. S. Usui et al., "Circadian changes in subfoveal choroidal thickness and the relationship with circulatory factors in healthy subjects," *Invest. Ophthalmol. Visual Sci.* **53**(4), 2300–2307 (2012).
9. X. Q. Li, M. Larsen, and I. C. Munch, "Subfoveal choroidal thickness in relation to sex and axial length in 93 Danish university students," *Invest. Ophthalmol. Visual Sci.* **52**(11), 8438–8441 (2011).
10. L. A. Yannuzzi, "Indocyanine green angiography: a perspective on use in the clinical setting," *Am. J. Ophthalmol.* **151**(5), 745–751 (2011).
11. R. F. Spaide, H. Koizumi, and M. C. Pozonni, "Enhanced depth imaging spectral-domain optical coherence tomography," *Am. J. Ophthalmol.* **146**(4), 496–500 (2008).
12. M. Hirata et al., "Macular choroidal thickness and volume in normal subjects measured by swept-source optical coherence tomography," *Invest. Ophthalmol. Visual Sci.* **52**(8), 4971–4978 (2011).
13. T. Torzicky et al., "Automated measurement of choroidal thickness in the human eye by polarization sensitive optical coherence tomography," *Opt. Express* **20**(7), 7564–7574 (2012).
14. D. C. Fernández, H. M. Salinas, and C. A. Puliafito, "Automated detection of retinal layer structures on optical coherence tomography images," *Opt. Express* **13**(25), 10200–10216 (2005).
15. M. Mujat et al., "Retinal nerve fiber layer thickness map determined from optical coherence tomography images," *Opt. Express* **13**(23), 9480–9491 (2005).
16. A. Mishra et al., "Intra-retinal layer segmentation in optical coherence tomography images," *Opt. Express* **17**(26), 23719–23728 (2009).
17. S. J. Chiu et al., "Automatic segmentation of seven retinal layers in SDOCT images congruent with expert manual segmentation," *Opt. Express* **18**(18), 19413–19428 (2010).
18. A. Ehnes, "Entwicklung eines Schichtsegmentierungsalgorithmus zur automatischen Analyse von individuellen Netzhautschichten in optischen Kohärenztomographie-B-Scans," PhD Thesis, Justus-Liebig-Universität Gießen, Germany (2014).
19. M. K. Garvin et al., "Automated 3-D intraretinal layer segmentation of macular spectral-domain optical coherence tomography images," *IEEE Trans. Med. Imaging* **28**(9), 1436–1447 (2009).
20. K. Li et al., "Optimal surface segmentation in volumetric images—a graph-theoretic approach," *IEEE Trans. Pattern Anal. Mach. Intell.* **28**(1), 119–134 (2006).
21. K. A. Vermeer et al., "Automated segmentation by pixel classification of retinal layers in ophthalmic OCT images," *Biomed. Opt. Express* **2**(6), 1743–1756 (2011).
22. V. Kajić et al., "Robust segmentation of intraretinal layers in the normal human fovea using a novel statistical model based on texture and shape analysis," *Opt. Express* **18**(14), 14730–14744 (2010).
23. A. R. Cho, Y. J. Choi, and Y. T. Kim, "Influence of choroidal thickness on subfoveal choroidal thickness measurement repeatability using enhanced depth imaging optical coherence tomography," *Eye* **28**(10), 1151–1160 (2014).
24. X. Ding et al., "Choroidal thickness in healthy Chinese subjects," *Invest. Ophthalmol. Visual Sci.* **52**(13), 9555–9560 (2011).
25. M. Esmaeelpour et al., "Three-dimensional 1060-nm OCT: choroidal thickness maps in normal subjects and improved posterior segment visualization in cataract patients," *Invest. Ophthalmol. Visual Sci.* **51**(10), 5260–5266 (2010).
26. M. Esmaeelpour et al., "Mapping choroidal and retinal thickness variation in type 2 diabetes using three-dimensional 1060-nm optical coherence tomography," *Invest. Ophthalmol. Visual Sci.* **52**(8), 5311–5316 (2011).

27. I. Flores-Moreno et al., "The relationship between axial length and choroidal thickness in eyes with high myopia," *Am. J. Ophthalmol.* **155**(2), 314–319 (2013).
28. Y. Ikuno et al., "Reproducibility of retinal and choroidal thickness measurements in enhanced depth imaging and high-penetration optical coherence tomography," *Invest. Ophthalmol. Visual Sci.* **52**(8), 5536–5540 (2011).
29. X. Q. Li et al., "Subfoveal choroidal thickness in 1323 children aged 11 to 12 years and association with puberty: the Copenhagen Child Cohort 2000 Eye study," *Invest. Ophthalmol. Visual Sci.* **55**(1), 550–555 (2014).
30. X. Q. Li et al., "Choroidal thickness in relation to birth parameters in 11- to 12-year-old children: the Copenhagen Child Cohort 2000 Eye study," *Invest. Ophthalmol. Visual Sci.* **56**(1), 617–624 (2015).
31. M. Lindner et al., "Choroidal thickness in geographic atrophy secondary to age-related macular degeneration," *Invest. Ophthalmol. Visual Sci.* **56**(2), 875–882 (2015).
32. R. Margolis and R. F. Spaide, "A pilot study of enhanced depth imaging optical coherence tomography of the choroid in normal eyes," *Am. J. Ophthalmol.* **147**(5), 811–815 (2009).
33. J. M. Ruiz-Moreno et al., "Macular choroidal thickness in normal pediatric population measured by swept-source optical coherence tomography," *Invest. Ophthalmol. Visual Sci.* **54**(1), 353–359 (2013).
34. J. W. Shin, Y. U. Shin, and B. R. Lee, "Choroidal thickness and volume mapping by a six radial scan protocol on spectral-domain optical coherence tomography," *Ophthalmology* **119**(5), 1017–1023 (2012).
35. D. A. Sim et al., "Repeatability and reproducibility of choroidal vessel layer measurements in diabetic retinopathy using enhanced depth optical coherence tomography," *Invest. Ophthalmol. Visual Sci.* **54**(4), 2893–2901 (2013).
36. S. Lee et al., "Comparative analysis of repeatability of manual and automated choroidal thickness measurements in nonneovascular age-related macular degeneration," *Invest. Ophthalmol. Visual Sci.* **54**(4), 2864–2871 (2013).
37. Y. Matsuo et al., "Comparisons of choroidal thickness of normal eyes obtained by two different spectral-domain OCT instruments and one swept-source OCT instrument," *Invest. Ophthalmol. Visual Sci.* **54**(12), 7630–7636 (2013).
38. D. Alonso-Caneiro, S. A. Read, and M. J. Collins, "Automatic segmentation of choroidal thickness in optical coherence tomography," *Biomed. Opt. Express* **4**(12), 2795–2812 (2013).
39. Z. Hu et al., "Semiautomated segmentation of the choroid in spectral-domain optical coherence tomography volume scans," *Invest. Ophthalmol. Visual Sci.* **54**(3), 1722–1729 (2013).
40. J. Tian et al., "Automatic segmentation of the choroid in enhanced depth imaging optical coherence tomography images," *Biomed. Opt. Express* **4**(3), 397–411 (2013).
41. L. Zhang et al., "Automated segmentation of the choroid from clinical SD-OCT," *Invest. Ophthalmol. Visual Sci.* **53**(12), 7510–7519 (2012).
42. L. Zhang et al., "Validity of automated choroidal segmentation in SS-OCT and SD-OCT," *Invest. Ophthalmol. Visual Sci.* **56**(5), 3202–3211 (2015).
43. V. Kajić et al., "Automated choroidal segmentation of 1060 nm OCT in healthy and pathologic eyes using a statistical model," *Biomed. Opt. Express* **3**(1), 86–103 (2012).
44. I. Boll, "Quadratische Kantenfilter zur Segmentierung von Bohrlogs," Diploma Thesis, Rheinische Friedrich-Wilhelms-Universität Bonn, Germany (1998).
45. N. B. Firoozye and V. Šverák, "Measure filters: an extension of Wiener's theorem," *Indiana Univ. Math. J.* **45**(3), 695–707 (1996).
46. S. Luckhaus, K. Räwer, and J. Rittscher, *A New γ-Convergent Approximation of the Mumford Shah Functional*, Rheinische Friedrich-Wilhelms-Universität Bonn, Germany; SFB 256, Preprint No. 517 (1997).
47. M. Wagner, "An application of quadratic measure filters to the segmentation of chorio-retinal OCT data," *J. Math. Imaging Vision* (submitted).
48. H. Walther, "Quadratische Kantenfilter," Diploma Thesis, Rheinische Friedrich-Wilhelms-Universität Bonn, Germany (1994).
49. H. Walther, "Rekonstruktion von Funktionen beschränkter Variation," PhD Thesis, Rheinische Friedrich-Wilhelms-Universität Bonn, Germany (1997).
50. P. Scheibe et al., "Parametric model for the 3D reconstruction of individual fovea shape from OCT data," *Exp. Eye Res.* **119**, 19–26 (2014).
51. P. Scheibe et al., "Analysis of foveal characteristics and their asymmetries in the normal population," *Exp. Eye Res.* **148**, 1–11 (2016).
52. T. Poulain et al., "The LIFE Child study: a population-based perinatal and pediatric cohort in Germany," *Euro. J. Epidemiol.*
53. *Spectralis HRA + OCT, User Manual Software Version 5.4*, Heidelberg Engineering GmbH, Heidelberg (2011).
54. *Biometer Lenstar LS 900, Instructions for Use*, 8th ed., Haag-Streit AG, Koeniz (2014).
55. *Spectralis, Spectralis Viewing Module, Software Version 4.0. Special Function: Exporting Raw Data*, Document revision 4.0-1E, Heidelberg Engineering GmbH, Heidelberg (2008).
56. C. Brune, H. Maurer, and M. Wagner, "Detection of intensity and motion edges within optical flow via multidimensional control," *SIAM J. Imaging Sci.* **2**(4), 1190–1210 (2009).
57. L. C. Evans, *Partial Differential Equations*, American Mathematical Society, Providence (1998).
58. http://www.mathworks.com/products/matlab/ (16 August 2016).
59. http://www.mathworks.com/products/image/ (16 August 2016).
60. http://www.mathworks.com/products/signal/ (16 August 2016).
61. W. Y. Yang et al., *Applied Numerical Methods Using MATLAB*, Wiley-Interscience; Hoboken (2005).
62. National Eye Institute, "Early treatment diabetic retinopathy study (ETDRS), Manual of Operations. Final Report 1979–1985," National Institution of Health/PHS, Bethesda, http://www.ntis.gov/search/product.aspx?ABBR=PB85223006 (16 August 2016).
63. Early Treatment Diabetic Retinopathy Study Research Group, "Grading diabetic retinopathy from stereoscopic color fundus photographs—an extension of the modied Airlie House classication. ETDRS report no. 10," *Ophthalmology* **98**, 786–806 (1991).
64. D. F. Garway-Heath et al., "Measurement of optic disc size: equivalence of methods to correct for ocular magnification," *Br. J. Ophthalmol.* **82**(6), 643–649 (1998).
65. J. M. Bland and D. G. Altman, "Statistical methods for assessing agreement between two methods of clinical measurement," *Lancet* **327**(8476), 307–310 (1986).
66. J. M. Bland and D. G. Altman, "Measuring agreement in method comparison studies," *Stat. Methods Med. Res.* **8**(2), 135–160 (1999).
67. J. M. Bland and D. G. Altman, "Applying the right statistics: analyses of measurement studies," *Ultrasound Obstet. Gynecol.* **22**(1), 85–93 (2003).
68. J. M. Schmitt, "Optical coherence tomography (OCT): a review," *IEEE J. Sel. Top. Quantum Electron.* **5**(4), 1205–1215 (1999).
69. G. Aubert and P. Kornprobst, *Mathematical Problems in Image Processing: Partial Differential Equations and the Calculus of Variations*, 2nd ed., Springer, New York (2006).
70. G. Aubert and J.-F. Aujol, "A variational approach to removing multiplicative noise," *SIAM J. Appl. Math.* **68**(4), 925–946 (2008).
71. J. Shi and S. Osher, "A nonlinear inverse scale space method for a convex multiplicative noise model," *SIAM J. Imag. Sci.* **1**(3), 294–321 (2008).
72. G. Steidl and T. Teuber, "Removing multiplicative noise by Douglas-Rachford splitting methods," *J. Math. Imaging Vision* **36**(2), 168–184 (2010).
73. L. Franek et al., "A discretization method for the numerical solution of Dieudonné-Rashevsky type problems with application to edge detection within noisy image data," *Optim. Control Appl. Methods* **33**(3), 276–301 (2012).
74. L. C. Evans and R. F. Gariepy, *Measure Theory and Fine Properties of Functions*, CRC Press, Boca Raton (1992).
75. T. F. Chan and J. Shen, *Image Processing and Analysis. Variational, PDE, Wavelet, and Stochastic Methods*, SIAM, Philadelphia (2005).

Patrick Scheibe received his MSc degree in computer science in 2007 from Leipzig University. For the following 9 years, he was head of the image processing core unit at the Translational Centre for Regenerative Medicine Leipzig. Since 2016, he is leading data analyst at the Saxonian Incubator for Clinical Translation. His research interests focus on the quantification and analysis of biomedical experiments. Currently, he concentrates on modeling of foveal structures based on OCT measurements.

Biographies for the other authors are not available.